Aerodynamic Shape Optimization of Common Research Model Wing–Body–Tail Configuration

Song Chen,* Zhoujie Lyu,† Gaetan K. W. Kenway,‡ and Joaquim R. R. A. Martins§
University of Michigan, Ann Arbor 48109, Michigan

Wing shape is one of the main drivers of aircraft aerodynamic performance, so most aerodynamic shape optimization efforts have focused solely on the wing. However, the performance of the full aircraft configuration must account for the fact that the aircraft needs to be trimmed. Thus, to realize the full benefit of aerodynamic shape optimization, one should optimize the wing shape while including the full configuration and a trim constraint. To evaluate the benefit of this approach, we perform the aerodynamic shape optimization of the Common Research Model wing–body–tail configuration using gradient-based optimization with a Reynolds-averaged Navier–Stokes model that includes a discrete adjoint implementation. We investigate the aerodynamic shape optimization of the wing with a trim constraint that is satisfied by rotating the horizontal tail. We then optimize the same wing–body configuration without the tail but with an added trim drag penalty based on a surrogate model we created before the optimization. The drag coefficient is minimized subject to lift and trim constraints. We found that considering the trim during optimization is a better approach than using a fixed-wing moment constraint. We also show that the trim drag surrogate model we created yields a minimum drag coefficient that is within 1.2 counts of the minimum drag coefficient obtained by rotating the tail to satisfy the trim constraint. However, we recommend rotating the tail within the optimization process to obtain the best possible performance.

I. Introduction

THE aerodynamic design of aircraft has benefited tremendously from the development of computational fluid dynamics (CFD) models, which have replaced much of the wind-tunnel testing previously performed and shortened the design cycle by making it easier to try design variations. The use of numerical optimization has the potential to further improve the aerodynamic design process by automating changes in the design and by seeking optimal designs. Since the design of three-dimensional shapes for aerodynamic performance requires hundreds of design variables, most researchers have resorted to tackling this problem using gradient-based optimizers with adjoint methods for computing the gradients, a technique pioneered by Jameson [1,2]. Given the ever increasing power of high-performance parallel computing, it is now possible to perform aerodynamic shape optimization based on the Reynolds-averaged Navier–Stokes (RANS) equations on complex geometries with hundreds of design variables [3,4].

The wing and horizontal tail play key roles in the aerodynamic performance of conventional aircraft configurations, since they directly affect the lift, drag, and moment of the aircraft. Since the benefit of drag reduction by optimizing the wing alone might not be realized once the full aircraft configuration is trimmed (i.e., when the aircraft is in equilibrium with respect to forces and moments), it is important to consider the trim constraint when performing the optimization. In typical transonic transport aircraft, trim is achieved by rotating the whole horizontal tail. This trim constraint can be

enforced without modeling the tail by constraining the moment of the wing alone [3]. Although this prevents the wing from producing too much of a pitchdown moment, limiting the trim drag, it does not allow for a tradeoff between wing aerodynamic performance and the trimming of the full aircraft. In addition, the aerodynamic load on the tail influences the circulation distribution of the whole aircraft in the Trefftz plane, directly influencing the induced drag. Moreover, the minimum induced drag for a given wing–tail system is not achieved with an elliptically loaded wing, since the optimal wing shape and twist are influenced by the horizontal tail design, so it is important to consider the whole system [5]. Thus, there is a need to consider the simultaneous analysis and design optimization of the wing and tail when performing aerodynamic shape optimization.

To address this need, we perform a series of aerodynamic shape optimizations of the Common Research Model (CRM) configuration. We have previously established that Euler-based models yield nonphysical designs for transonic wings [6], and thus we use RANS with a Spalart–Allmaras (SA) turbulence model exclusively. The investigations in this paper aim to answer several questions related to the trim of full configurations. First, we explore the differences in the results obtained by optimizing the aircraft with and without trim constraints and with and without a horizontal-tail shape design. Second, we investigate how close we can get to the true optimum by optimizing the full configuration with the shaping of the wing in the presence of the body only and by incorporating a trim penalty based on a value from a trimmed drag polar of the whole configuration.

Many researchers have investigated the design optimization of the wing only, and a few others have studied its design optimization within a more complex configuration such as a wing–body or wing–body–tail configuration. However, the influences of the horizontal-tail shape and the trimming have not yet been investigated in detail with RANS CFD. In this paper, we present the results of the lift-constrained drag minimization of the CRM wing–body–tail configuration [7] using RANS CFD, with shape optimization of both the wing and tail simultaneously.

Aerodynamic shape optimization with gradient-based optimizers has been extensively investigated in the last few decades [8–12,3,4,]. Several researchers have investigated a RANS-based single-point benchmark developed by the AIAA Aircraft Design Optimization Discussion Group, which consists of shape optimization of the CRM wing alone [3,13–15], but trim considerations for all these studies were limited to a pitch moment coefficient constraint.

A few studies have considered the trimmed CRM configuration in the context of aerostructural design optimization, in which both the

*Visiting Scholar, Department of Aerospace Engineering. Student Member AIAA.

†Ph.D. Candidate, Department of Aerospace Engineering. Student Member AIAA.

‡Research Investigator, Department of Aerospace Engineering. Member AIAA.

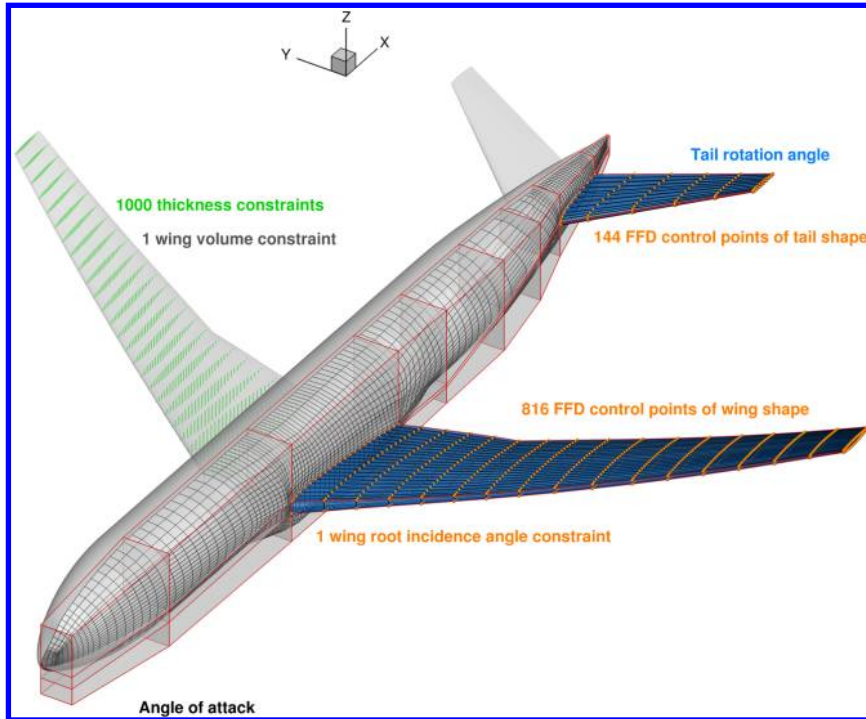§Professor, Department of Aerospace Engineering. Associate Fellow AIAA.

Fig. 1 The design variables consist of the z coordinates of the free-form deformation points on both the wing and the horizontal tail.

aerodynamic shape and structural sizing are optimized [16,17]. Flying wing configurations, such as the blended wing–body (BWB), exhibit a strong coupling between the aerodynamic performance and trim, since the wing must be able to trim the moment on its own, while maintaining longitudinal stability [18]. The aerodynamic shape optimization of BWB configurations including trim and stability was studied by Lyu and Martins [4]. Euler-based aerodynamic shape optimization for high-speed civil transport was studied by Cliff et al. [19], in which simultaneous multipoint design vs sequential cruise-point design followed by trim optimization at transonic conditions was performed. For tail design optimization, several investigations have addressed conceptual-level design, such as the tail sizing, dihedral, and load [5,20,21], but few studies have considered the trim [19,17]. The motivation for the present work is that there is currently no thorough study of full-configuration RANS-based aerodynamic shape optimization using the tail rotation to trim the aircraft and the influence of the trim constraint on the design.

In this paper, we choose the 4th Drag Prediction Workshop (DPW-4) CRM wing–body–tail configuration as our baseline model [7]. The reason for choosing this configuration is that the DPW-4 CRM is representative of a conventional wide-body commercial transport aircraft, which includes a supercritical wing, a wing–body fairing, and a horizontal tail. The horizontal tail was designed to satisfy

typical stability and control requirements [7], so the DPW-4 CRM is suitable for this investigation.

This paper is organized as follows. In Sec. II, we describe the numerical tools used in this work, and in Sec. III, we introduce the problem formulation, baseline geometry, and CFD mesh. In Sec. IV, we present the single-point wing aerodynamic shape optimization without a trim constraint, and in Sec. V, we discuss the optimization with the trim constraint. In Sec. VI, we present a single-point wing aerodynamic shape optimization without the tail, using a surrogate model for the tail trim penalty. Then, in Sec. VII, we present a single-point wing aerodynamic shape optimization without the tail but with a predetermined lift and moment constraint. Finally, in Secs. VIII and IX, we discuss a simultaneous wing and tail shape optimization with and without the trim constraint.

II. Methodology

This section describes the numerical tools and methods used for the optimization studies. These tools are components of the framework for multidisciplinary design optimization of aircraft configurations with high fidelity (MACH) [6,22]. MACH can perform the simultaneous optimization of aerodynamic shape and structural sizing variables considering aeroelastic deflections [23].
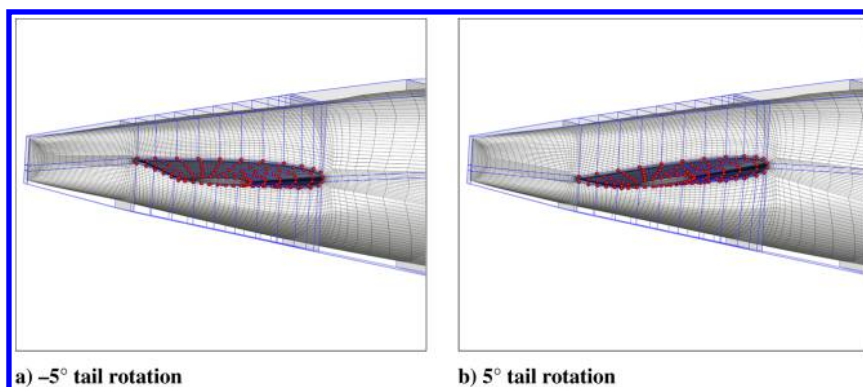

Fig. 2 A sub-FFD block rotates as a solid body to emulate the tail rotation used to trim the aircraft.
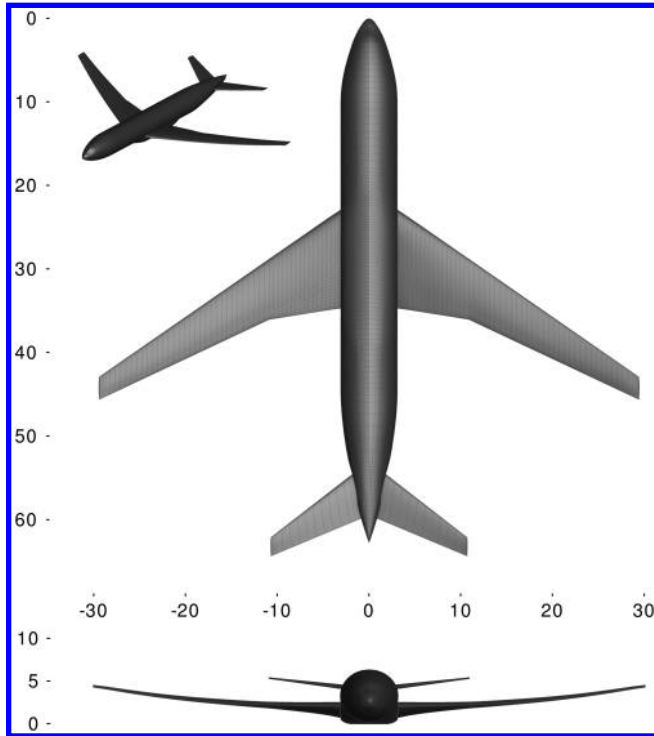
Fig. 3   CRM baseline geometry.

However, in this paper, we focus solely on aerodynamic shape optimization with no structural considerations.

A. Geometric Parameterization

Both the wing and the tail geometries are parameterized using the free-form deformation (FFD) volume approach [24]. The FFD volume parameterizes the changes of the embedded geometry rather than the geometry itself, resulting in a more efficient and compact set of geometry design variables, thus making it easier to manipulate complex geometries. Any geometry may be embedded inside the volume by performing a Newton search to map the parameter space to physical space. All geometric changes are performed on the outer boundary of the FFD volume. Any modification of this outer boundary can be used to indirectly modify the embedded objects. The key assumption of the FFD approach is that the geometry has constant topology throughout the optimization process, which is usually the case for aerodynamic design optimization. In addition, since FFD volumes are trivariate B-spline volumes, the sensitivities of any point inside the volume can be efficiently computed.

Figure 1 shows the FFD volume and the geometric control points for the aerodynamic shape optimization for the wing–body–tail configuration. The whole aircraft is enveloped by 28 FFD volumetric blocks; one of these parameterizes the wing, and another parameterizes the tail.

The wing is parameterized using 816 design variables that perturb the shape, which are the z coordinates of the FFD control points. The wing control points are distributed on the FFD volume surface in a regular grid with 17 spanwise by 24 chordwise points, with two layers controlling the upper and lower surfaces separately, as shown in Fig. 1. Since the transonic wing aerodynamic performance is sensitive to the leading-edge shape, the chordwise FFD control points are not distributed uniformly: there are more control points with smaller spacing around the leading edge to provide finer shape parameterization in that region. The wing root incidence angle is constrained to be fixed. Another 144 design variables parameterize the tail shape.

Most modern airliners achieve a moment equilibrium by rotating the whole horizontal tail, which generates a pitching moment to trim the aircraft. We implemented this variable by rotating a sub-FFD
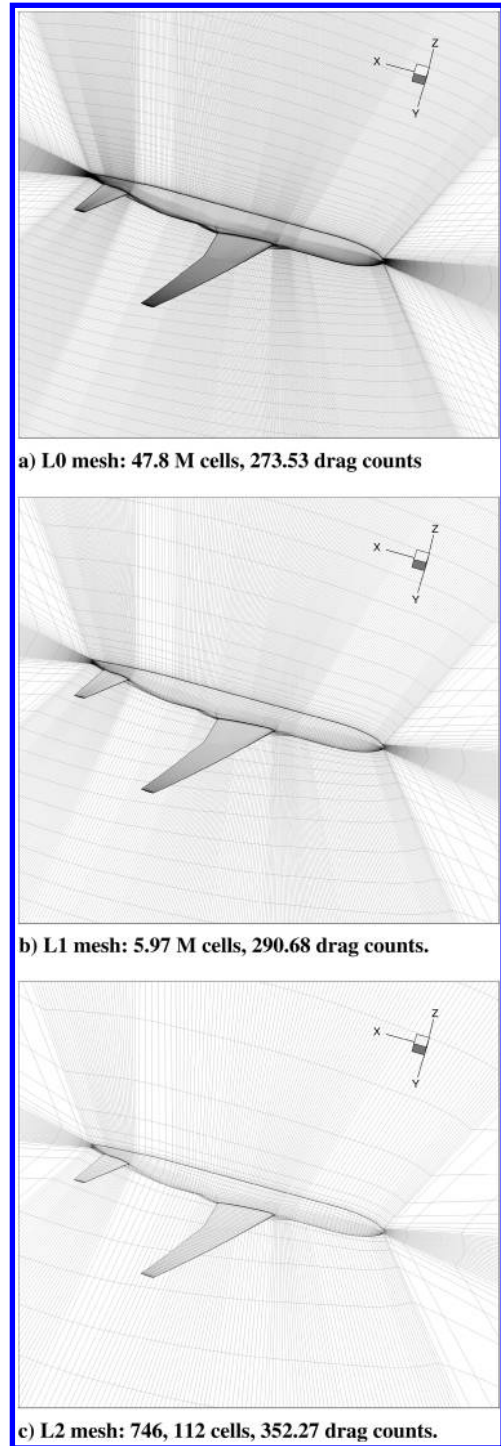

a) L0 mesh: 47.8 M cells, 273.53 drag counts

b) L1 mesh: 5.97 M cells, 290.68 drag counts.

c) L2 mesh: 746, 112 cells, 352.27 drag counts.

Fig. 4   O-H meshes of varying sizes generated using ICEM-CFD.

block that surrounds the horizontal tail, as illustrated in Fig. 2. The axis for the solid rotation of the tail is at the 40% chord length of the tail root section and is normal to the symmetry plane. The tail–body

Table 1   Mesh convergence study data

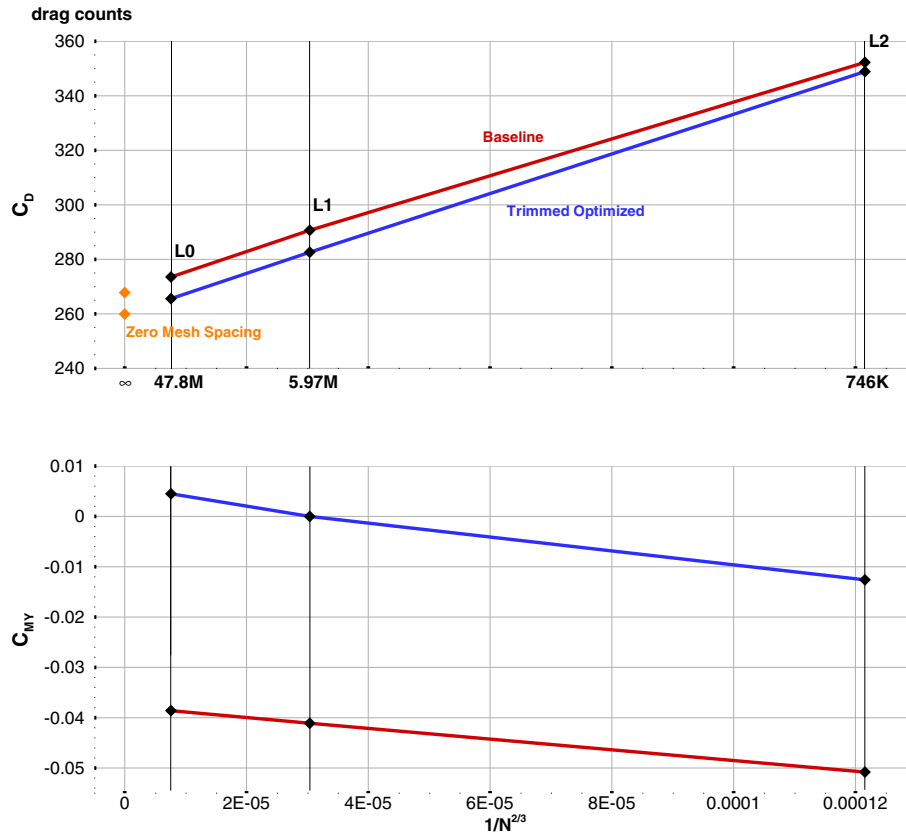| Mesh level	Cell number, N	C_D	y^+	C_L	C_{M_y}	α
$h = 0$	∞	0.026581	— —	— —	— —	— —
L0	47,751,168	0.027353	0.996	0.50000	−0.0386	2.332
L1	5,968,896	0.029068	2.744	0.50000	−0.0411	2.411
L2	746,112	0.035227	5.244	0.50000	−0.0508	2.551

Fig. 5   Mesh convergence for drag and moment coefficients of the baseline and single-point trimmed optimum (Case 2).

intersection is free to change as the tail rotates, just as in the case of real aircraft.

B.   Mesh Perturbation

Since FFD volumes modify the geometry during the optimization, we must perturb the CFD mesh to solve for the modified geometry. The mesh perturbation scheme used in this work is a hybridization of the algebraic and linear elasticity methods [24]. The idea behind the hybrid warping scheme is to apply a linear-elasticity-based warping scheme to a coarse approximation of the mesh to account for large, low-frequency perturbations and to use the algebraic warping approach to attenuate small, high-frequency perturbations.

C.   CFD Solver

For the CFD, we use the SUmb flow solver [25], which is a finite-volume, cell-centered multiblock solver for the compressible Euler, laminar Navier–Stokes, and RANS equations (steady, unsteady, and time periodic). SUmb provides options for a variety of turbulence models with one, two, or four equations and options for adaptive wall functions. The Jameson–Schmidt–Turkel scheme [26] is used for the spatial discretization. The mean flow is solved using a residual-averaged explicit multistage Runge–Kutta method along with a geometric multigrid technique. A segregated SA one-equation model is used to model the turbulence. We have developed a discrete adjoint method for the RANS equations for the efficient computation of the gradients required for the optimizations [6]. The adjoint implementation supports both the full-turbulence and frozen-turbulence modes, but in the present work, we use the full-turbulence adjoint exclusively. We solve the adjoint equations with the preconditioned generalized minimal residual method (GMRES) [27] using the portable, extensible toolkit for scientific computation (PETSc) [28,29].[¶]

D.   Optimization Algorithm

Because of the high computational cost of CFD solutions, it is critical to choose an efficient optimization algorithm that requires a low number of function calls. Gradient-free methods, such as genetic algorithms, have a higher probability of getting close to the global minimum for cases with multiple local minima, but slow convergence and the large number of function calls make gradient-free aerodynamic shape optimization infeasible with the current computational resources, especially for large numbers of design variables. Since we require hundreds of design variables, we use a gradient-based optimizer combined with adjoint gradient evaluations to solve the problem efficiently. The local minima issue of the gradient-based aerodynamic shape optimization has been explored by Lyu et al. [3], who concluded that numerical local minima exist, but they are restricted to a small space around the optimum, with differences in drag coefficients of the order of a tenth of a drag count. These small differences are negligible.

Table 2   Summary of the optimization formulations

Case	Configuration	Design variables	Constraints
1	Wing–body–tail	AoA, wing shape	Geometric $C_L = 0.5$
2	Wing–body–tail	AoA, wing shape tail rotation	Geometric $C_L = 0.5$, $C_M = 0$
3	Wing–body	AoA, wing shape	Geometric $C_L = 0.5$, $C_M = 0$ (surrogate)
4	Wing–body	AoA, wing shape	Geometric $C_L = 0.5256$, $C_M \geq -0.0996$
5	Wing–body–tail	AoA, wing shape, tail shape	Geometric $C_L = 0.5$
6	Wing–body–tail	AoA, wing shape, tail shape, tail rotation	Geometric $C_L = 0.5$, $C_M = 0$

We use the optimization algorithm SNOPT (sparse nonlinear optimizer) [30] through the Python interface pyOpt [31]. SNOPT is a gradient-based optimizer that implements a sequential quadratic programming method; it is capable of solving large-scale nonlinear optimization problems with thousands of constraints and design variables.

III. Problem Formulation

We now present the details of the baseline geometry as well as the optimization formulations for the various cases that we solved.

A. Baseline Geometry

As previously mentioned, the baseline geometry is that of the DPW-4 CRM, which is a wing–body–tail configuration, with the tail rotation set to zero. The development of the CRM is detailed by Vassberg et al. [7], and the geometry is shown in Fig. 3. The reference point is at 25% mean aerodynamic chord (MAC), which corresponds to the position of the center of gravity. The coordinates for this point are $(x, y, z) = (33.677, 0.0077, 4.520)$ m. The reference area is 383.69 m^2, and the reference length (MAC) is 7.005 m. The nominal flight condition of the CRM is a cruise Mach number of 0.85 with a nominal lift coefficient of $C_L = 0.50$. The Reynolds number is
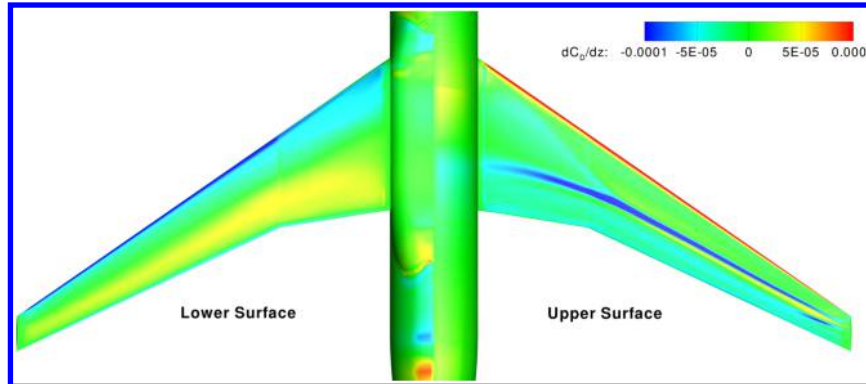

Fig. 6 Drag coefficient sensitivity contour of the baseline configuration with respect to shape perturbation in the z direction.
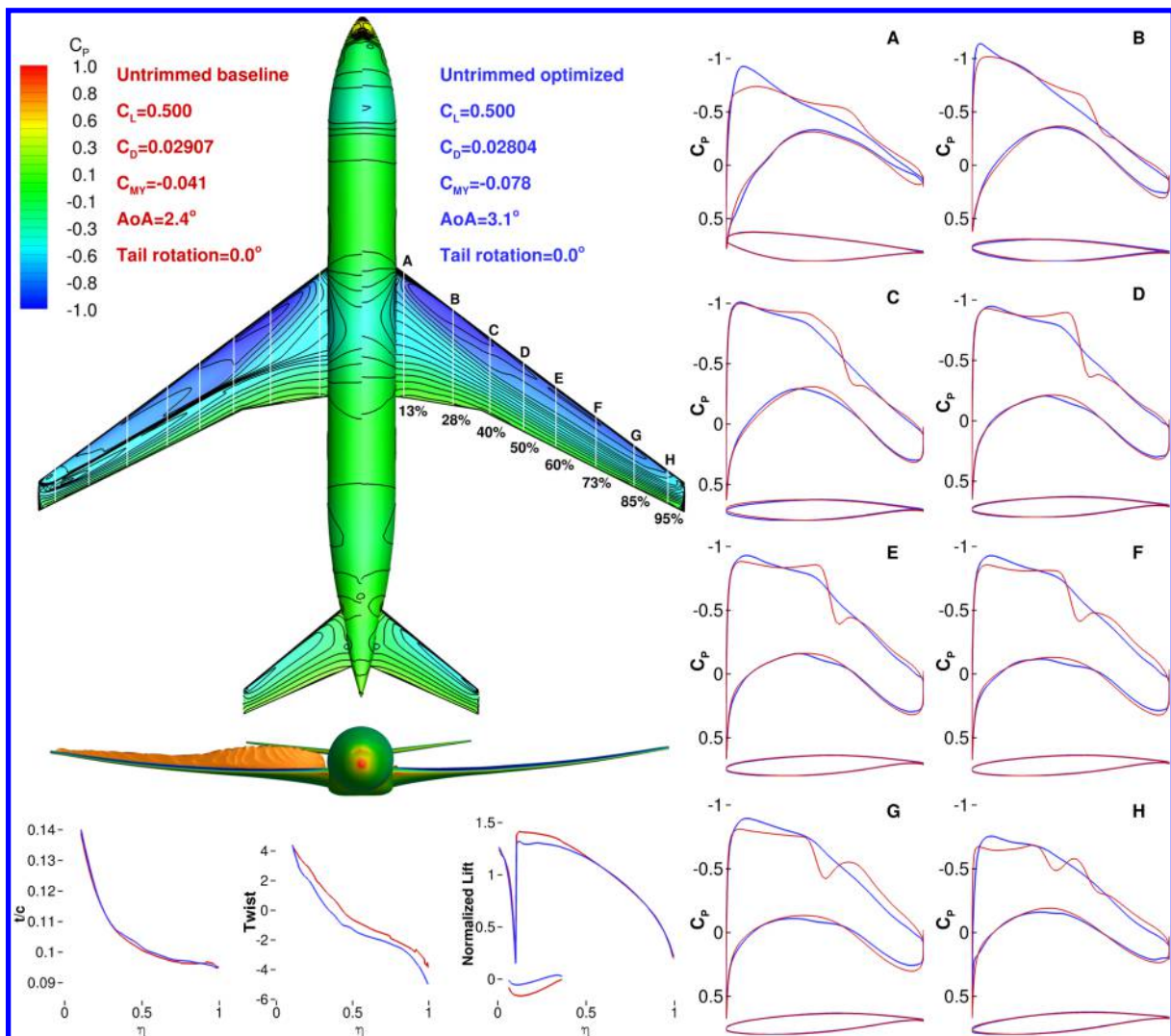

Fig. 7 Comparison of the single-point untrimmed optimization (Case 1; right) with the baseline configuration (left).
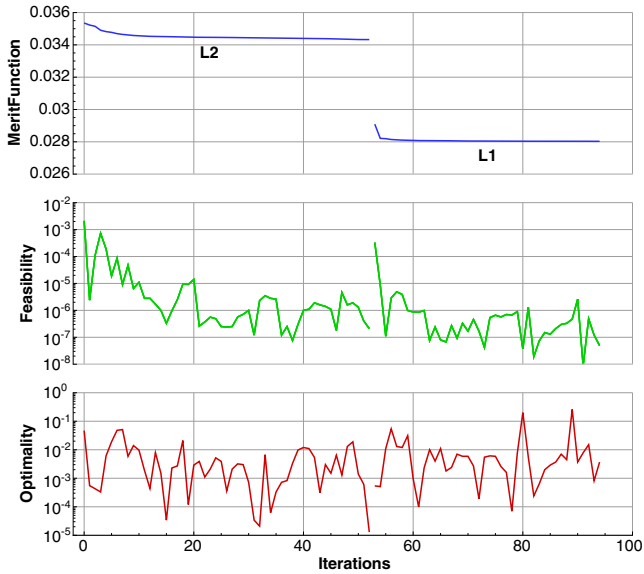
Fig. 8 Convergence history for the single-point untrimmed case.

selected as 5 million based on the mean aerodynamic chord, which is consistent with the wind-tunnel test.

B. Mesh Convergence Study

The CFD structured mesh is generated with ANSYS ICEM-CFD and consists of a multiblock structured node-matching mesh with O-H topology; the total number of blocks is 1018. We first perform a mesh convergence study with different coarsening levels. The flow condition for the convergence study is the nominal cruise flow condition $(M = 0.85$, $Re = 5 \times 10^6$, and $C_L = 0.5)$. In the optimization, we use the same multilevel mesh methodology that we used previously to accelerate the design optimization [32]. The finest mesh that is directly generated by ICEM-CFD has about 47.8 million cells (denoted the L0 mesh). This mesh is uniformly coarsened twice, resulting in a 5.97 million cell mesh (L1) and a 746,000 cell mesh (L2). The surface and the symmetry plane for the L0, L1, and L2 meshes are shown in Fig. 4. The mesh size, y_{max}^+ values, C_L values, C_D values, and C_{M_y} values at the nominal operating condition for these three mesh levels are listed in Table 1. Figure 5 shows the drag convergence plot with respect to $1/N^{2/3}$, where N is the number of mesh cells. We also compute the zero-mesh spacing drag using Richardson's extrapolation, which estimates the drag value as the mesh spacing approaches zero [33]. The zero-mesh spacing drag coefficient is 267.8 counts for the baseline CRM. As
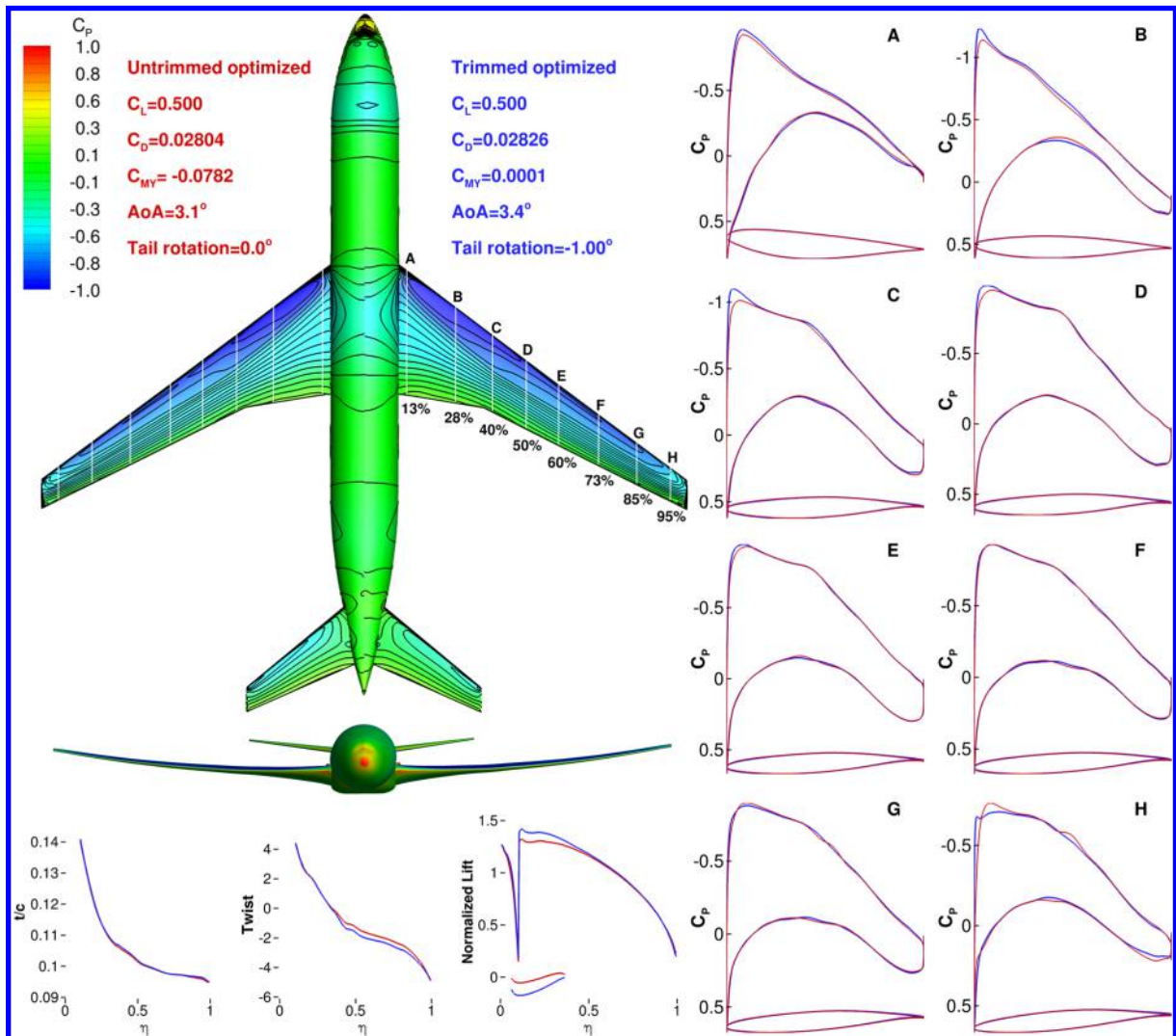

Fig. 9 Comparison of the single-point trimmed optimal configuration (Case 2; right) with the untrimmed optimized configuration (Case 1; left).

shown in Fig. 5, the drag convergence curve is linear and shows a consistent trend. After considering the tradeoff between computational time and accuracy, we decided to use the two coarse mesh levels (L1 and L2) for the optimizations. Since we perform optimizations that include tail rotation and tail shape changes, which could influence the longitudinal stability of the aircraft, we computed $-\partial C_M/\partial C_L$ of the baseline geometry at the cruise condition. This is 30% and indicates that a static margin of 30% MAC will be obtained when the center of gravity is at the location of the referenced point.

C. Optimization Formulation

The objective of the optimization problem is to minimize the drag coefficient of the aircraft, subject to a lift coefficient constraint ($C_L = 0.5$). The angle of attack is the primary design variable that is used to satisfy the lift coefficient constraint. The shape design variables are as described in Sec. III.A. Recall that there is a total of 816 wing shape variables and 144 tail shape variables when applicable. The horizontal tail rotation angle, as previously explained, is an additional design variable for the cases that enforce trim ($C_M = 0$) as a constraint using this variable. The bounds for the tail rotation values are set to ± 5 deg.

The geometric constraints are as follows. The wing internal volume is constrained to be no less than that for the baseline. In addition, we impose 1000 thickness constraints at points over a uniform grid on the wing with 25 chordwise by 40 spanwise locations, as shown in Fig. 1. These thickness constraints ensure that the thicknesses at these locations are no less than the corresponding baseline thickness, which guarantees the corresponding structural height. In addition, the thickness constraints that are at the leading edge (first 4% chord) of the wing ensure that the leading-edge radius is not reduced significantly, so that the low-speed performance is maintained to a certain extent. All of the previous constraints ensure that the optimization yields a practical design.

In this paper, we solve a series of six cases to gain an understanding of the effect of including trim in aerodynamic shape optimization. The six cases are summarized in Table 2. In Case 1, we optimize the wing–body–tail configuration with wing shape design variables. In Case 2, we add the tail rotation design variable and the trim constraint. In Cases 3 and 4, we create a wing–body configuration by removing the tail from the original wing–body–tail configuration. In Case 3, we enforce C_L and C_M constraints using a surrogate model for the trim drag; and in Case 4, C_L and C_M are fixed to the values of the wing–body component from the trimmed baseline geometry. Finally, we
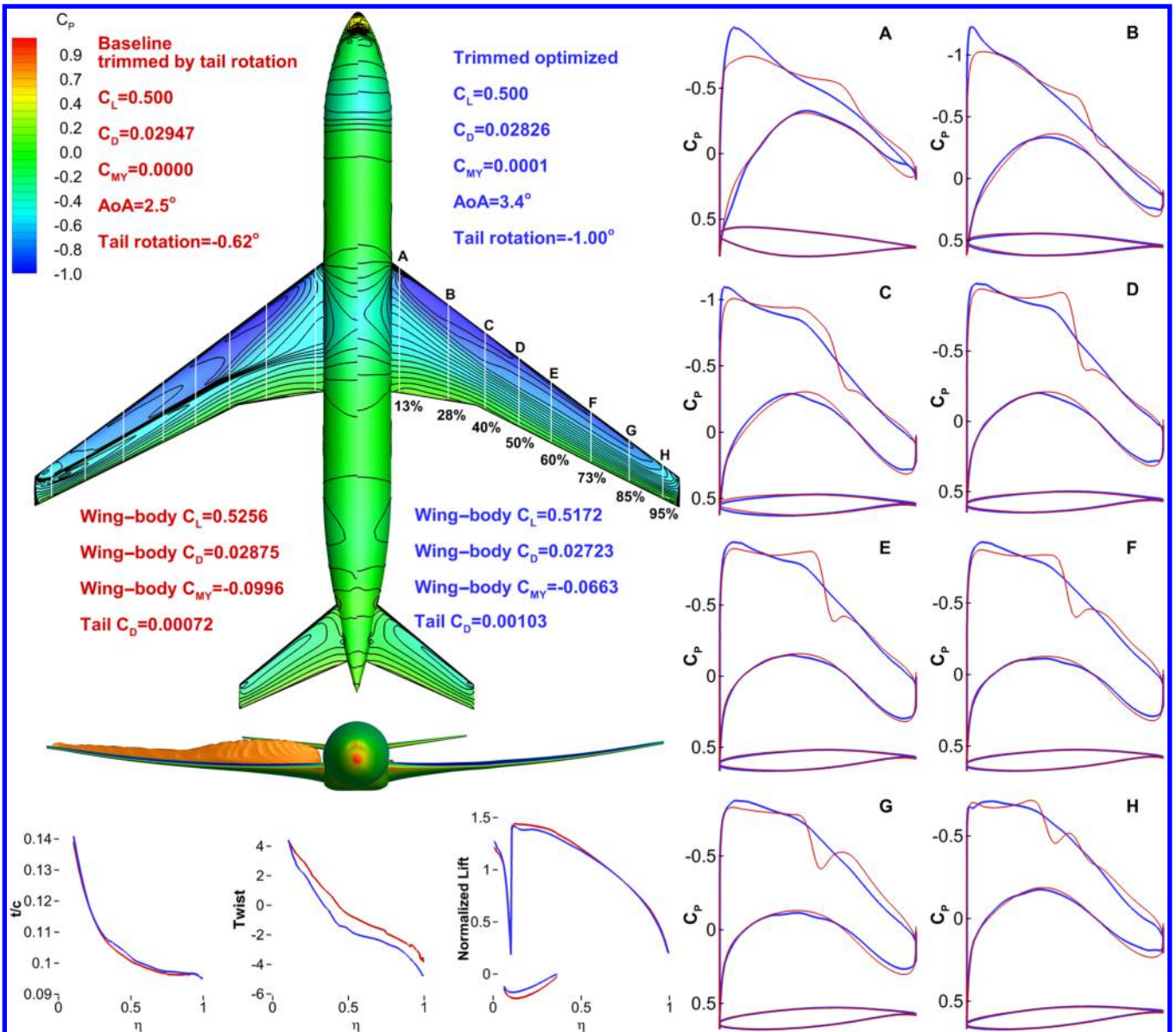

Fig. 10   Comparison of the single-point trimmed optimal configuration (Case 2; right) with the trimmed baseline (left).

add the tail shape design variables to the wing–body–tail configuration optimization without the trim constraint (Case 5) and with that constraint (Case 6).

D. Surface Sensitivity on Baseline Geometry

We first perform a sensitivity analysis of the baseline geometry at the nominal cruise condition. Figure 6 shows the derivatives of C_D with respect to shape variations in the z direction on the wing and fuselage; the changes in z are positive upward, irrespective of the local orientation of the surface. In Fig. 6, we can see that one of the areas with the highest sensitivity to C_D is the shock wave region on the wing upper surface. This is expected, since shaping in this area could drastically reduce the wave drag, and it indicates that the optimization will first try to eliminate the shock in order to reduce C_D.

IV.   Case 1: Optimization of Wing Without Moment Constraint

In this section, we present the results of the single-point aerodynamic shape design optimization of the CRM wing–body–tail configuration, in which only wing shape design variables are varied with no enforcement of a moment constraint. Two mesh levels (L2 with 746,112 cells and L1 with 5.97 million cells) are used in the multilevel optimization. This case is run with 64 processors for the L2 mesh and 256 processors for the L1 mesh. The design variables in this case are the wing shape design variables and the angle of attack, with lift coefficient and geometric constraints. The tail rotation is not a design variable, since we make no attempt to trim the configuration. The optimized wing for the L1 mesh has a drag 3.54% lower than that for the baseline geometry. The drag decreased from 290.7 counts to 280.4 counts at the nominal flow condition. The negative pitching moment coefficient increased from -0.041 to -0.078, and the angle of attack increased from 2.4 to 3.1 deg. Figure 7 shows a comparison of the baseline and optimized wings.

The convergence history of the optimization is shown in Fig. 8 for the two-level optimization process. The feasibility and optimality parameters used in SNOPT are defined by Gill et al. [30]. In SNOPT, feasibility is defined via the maximum constraint violation, which is a measure of how closely the nonlinear constraints are satisfied. Optimality refers to how closely the current point satisfies the first-order Karush–Kuhn–Tucker conditions. The optimality typically
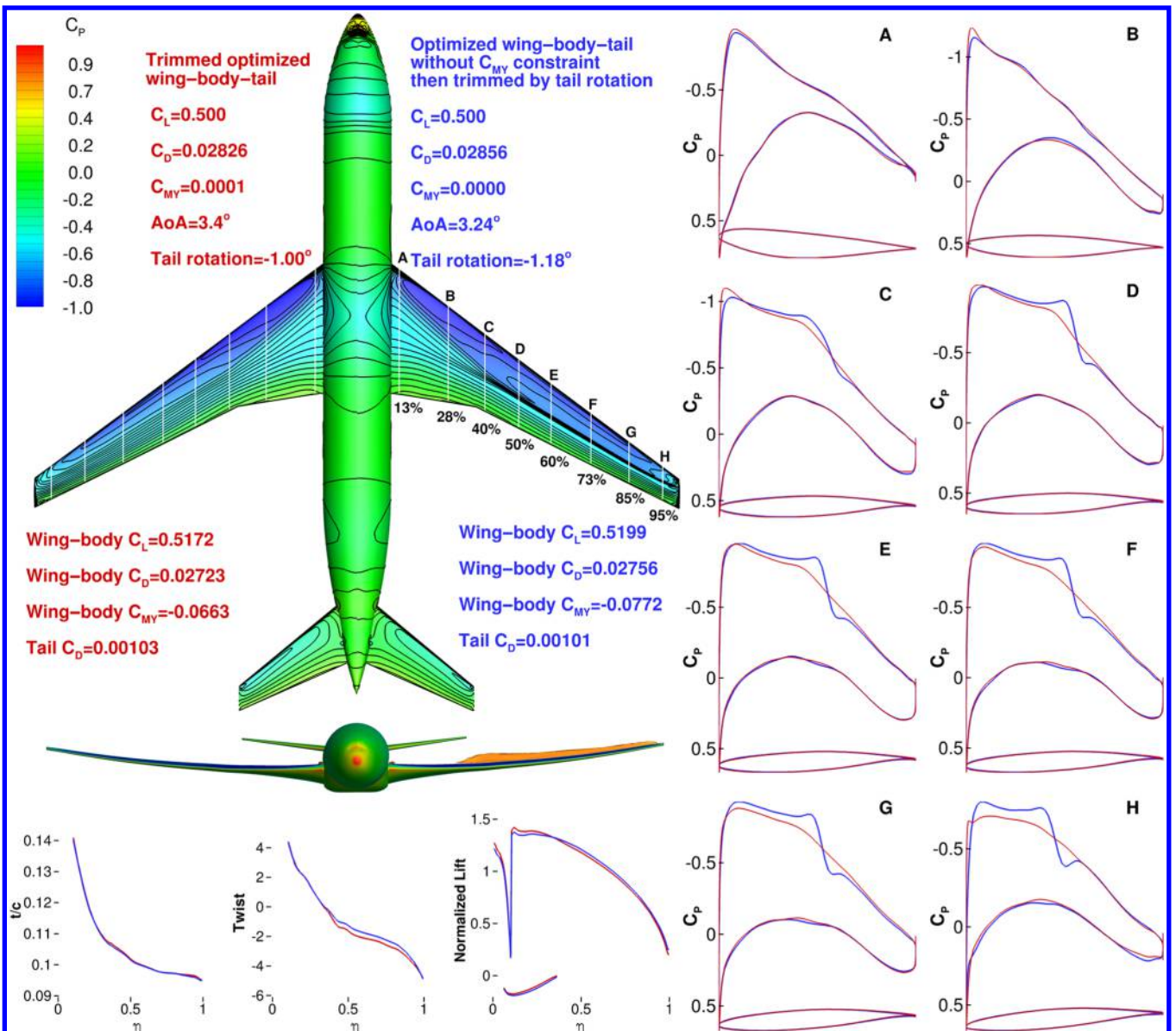

Fig. 11   Comparison of the optimized wing–body–tail without trim constraint and trimmed by rotating tail after optimization (Case 1; right) with the trim-constrained optimized wing–body–tail (Case 2; red).
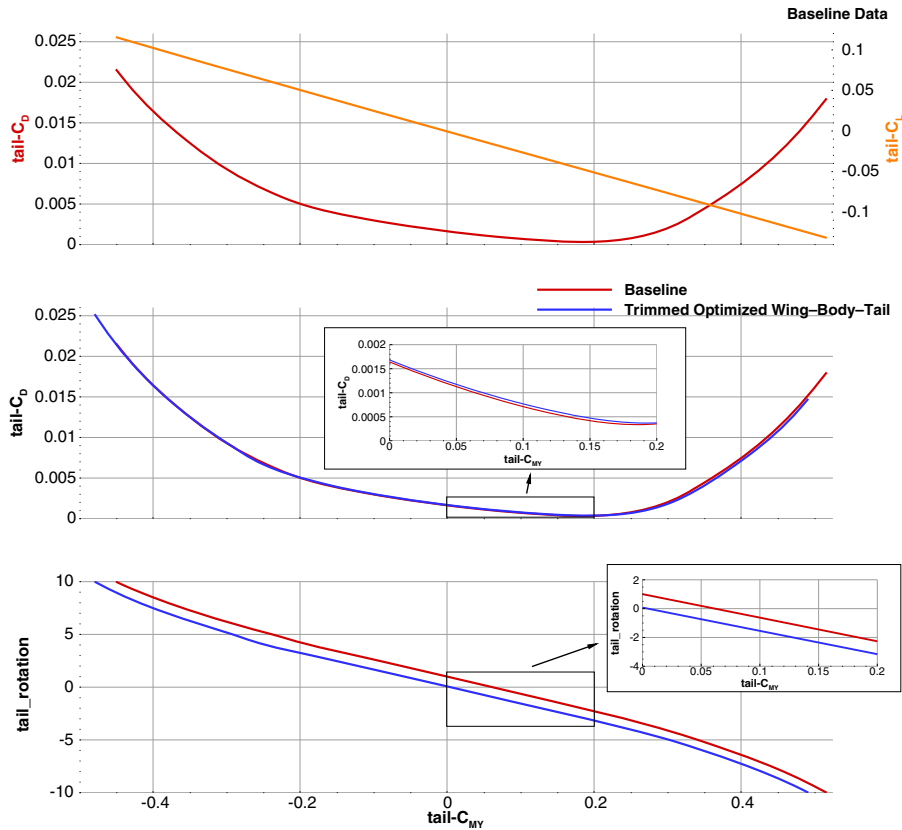
Fig. 12   Tail drag and lift coefficients vs tail moment for the baseline configuration for a fixed total lift coefficient ($C_L = 0.5$) and comparison with the trimmed optimized configuration.

decreases by two to three orders of magnitude for the first mesh level optimization, while the feasibility converges to a tolerance of 10^{-7} or less. Toward the end of the optimization iterations, the drag coefficient varies by less than 0.01%.

The left side of Fig. 7 shows a comparison of the upper surface pressure coefficient contour, in which the baseline wing exhibits a front of closely spaced pressure contour lines spanning a significant portion of the wing, indicating a shock wave. On the other side, the optimized wing exhibits parallel pressure contour lines with roughly equal spacing, indicating a nearly shock-free solution. Below the contour comparison plot, the front view shows the shock region above the baseline wing. The shock rendering method is that presented by Lovely and Haimes [34]. The basic idea is to use the pressure gradient to find the value of the Mach number normal to a shock in order to form an isosurface for rendering the shock. This approach was also implemented in Plot3D [35]. Since the shock surface normal is aligned with the pressure gradient vector, the Mach number in the direction of this vector is the normal Mach number. A shock is then located where this normal Mach number is greater than or equal to unity. The optimized wing does not show a shock. The lower left of Fig. 7 gives a comparison of the relative thickness, wing twist distribution, and normalized lift along the span.

The right side of Fig. 7 shows a comparison of multiple airfoil section geometries and the corresponding pressure coefficient distributions. These plots confirm that the shock is eliminated by the optimization, with the upper surface pressure recovering smoothly from the leading edge to trailing edge in the optimized wing, in contrast with the shock present on the baseline wing. Since no moment constraint is imposed in this case and we did not have the tail rotation as a design variable, the negative pitching moment is increased from −0.041 to −0.078. The lift distributions of the optimized wing and the baseline wing are shown by separating the lift on the wing–body and the tail. These distributions show that both the negative lift on the tail and the positive lift on the wing have

decreased. Since the tail cannot be rotated, the angle of attack increases from 2.41 to 3.1 deg in part because the optimizer increases this angle to decrease the negative lift on the tail, which also decreases the lift on the wing to maintain the equilibrium of lift $C_L = 0.5$. The reduced lift on the wing makes it easier for the optimizer to reduce the wing drag and achieve a shock-free design. To a certain extent, the optimizer is using the angle of attack to achieve a tradeoff between the lift on the wing and that on the tail.
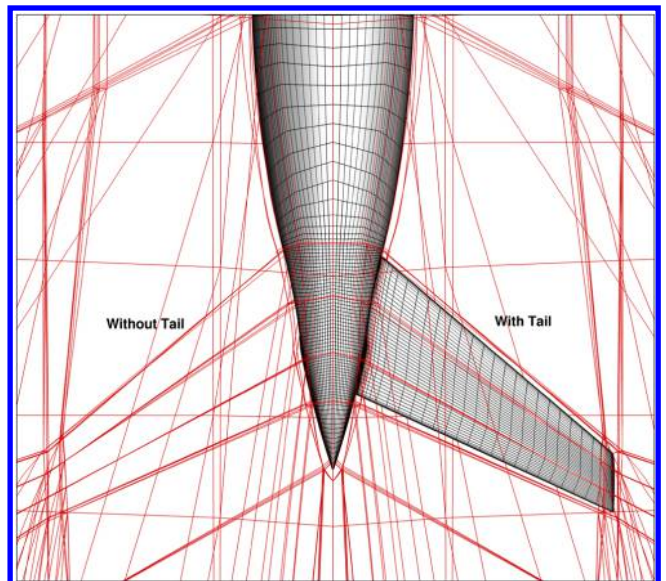

Fig. 13   Comparison of mesh around the tail for the wing–body and wing–body–tail configurations.

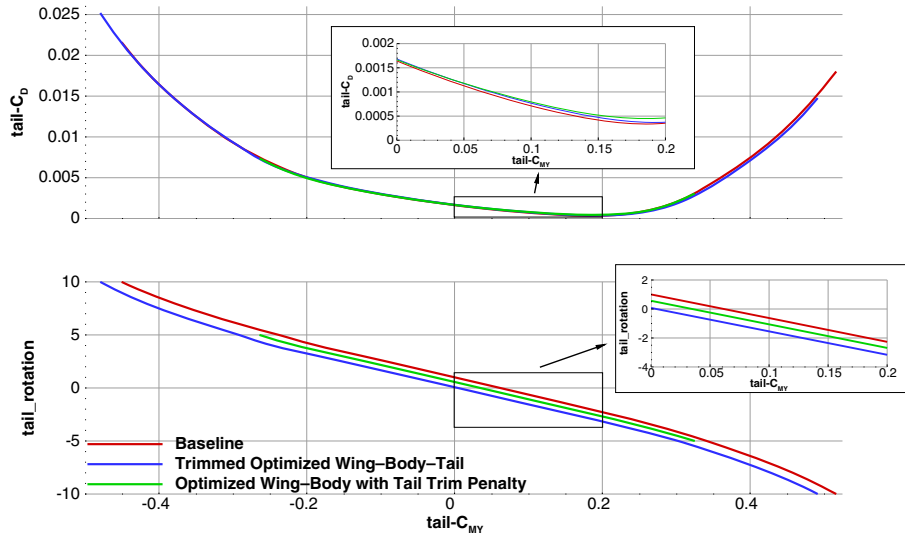**Fig. 14 Tail drag and lift coefficients vs tail moment for the baseline configuration for a fixed total lift coefficient ($C_L = 0.5$) and comparison of the trimmed optimized configuration and the optimized wing–body with tail trim penalty.**
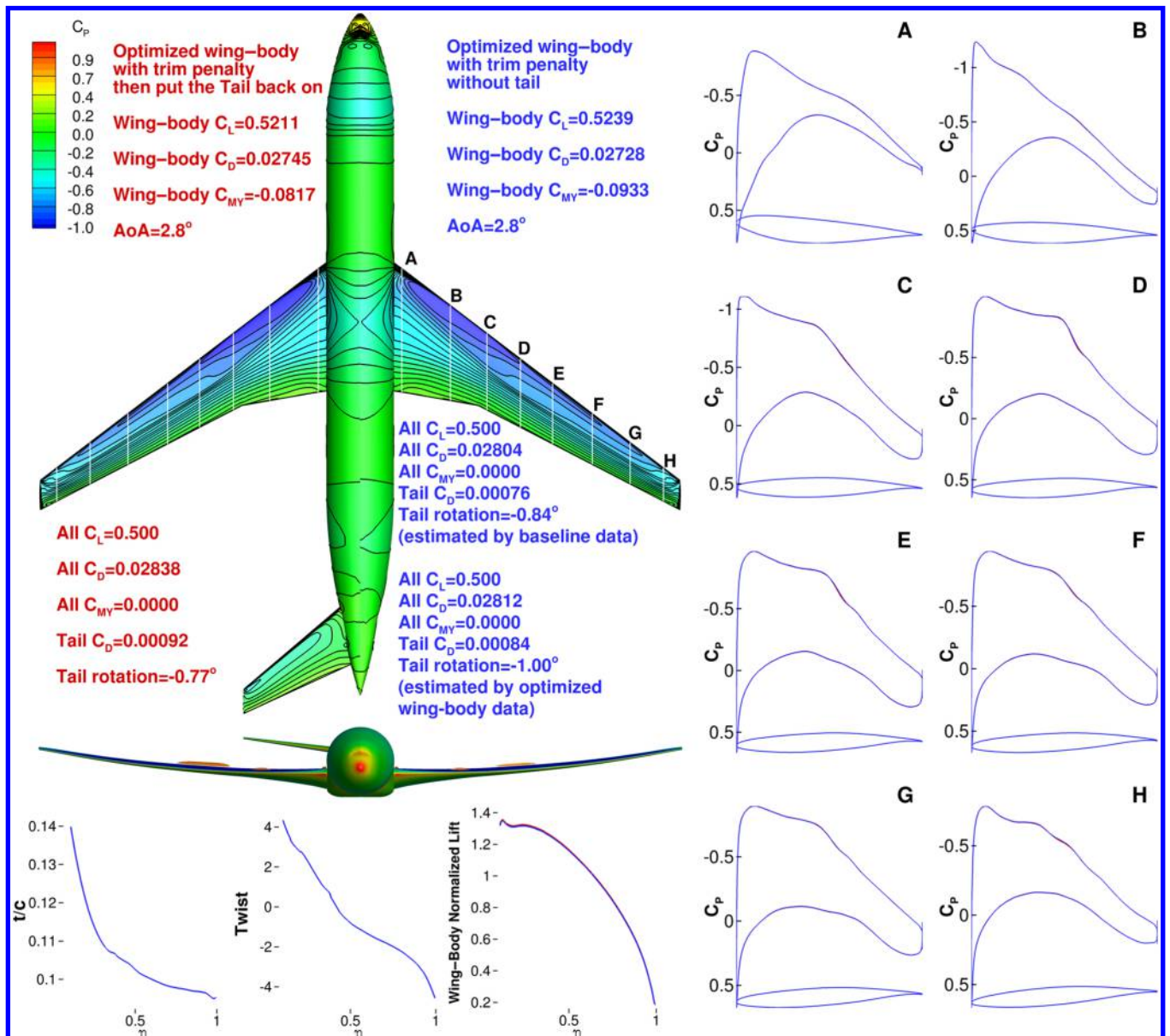

Fig. 15 Comparison of the optimized wing–body with surrogate trim drag penalty (Case 3; right) and the same configuration with the tail added back on and trimmed (Case 3; left).

From these results, we conclude that optimization on the wing only without a moment constraint is able to achieve a shock-free design with considerable drag reduction. However, the negative pitching moment increased considerably, which suggests that it would lead to a higher drag if we trimmed this configuration. We confirm this speculation in the next section.

V. Case 2: Optimization of Wing with Tail Rotation and Trim Constraint

We now perform an optimization in which the trim is achieved by adding a pitching moment constraint and the tail rotation angle as an additional design variable. Figure 9 compares the trim-constrained optimized wing with the untrimmed optimized wing. The optimized tail rotation angle for the trimmed optimization is −1 deg. The drag value of the trimmed optimization increases by 2.2 drag counts relative to the untrimmed optimized wing, but the total drag is still lower than that of the baseline, which is untrimmed. The angle of attack further increases from 3.1 to 3.4 deg. The pressure coefficient contour of this trim-constrained optimal wing is similar to that of the untrimmed wing, and it also shows a shock-free optimized solution. From the section pressure coefficient plots, we can see that the suction peak of the inboard sections increases, which is consistent

with the increasing lift on the inboard wing to partially compensate for the increased negative lift on the tail required to trim the configuration.

We perform a drag convergence study on this optimized geometry and compare the convergence to that of the baseline geometry. The optimization is done on the L1 mesh, and then the design variables given by this optimization are applied to the L2 and L0 meshes to obtain results for the three mesh levels with the same optimized geometry. As we can infer from Fig. 5, when the optimized geometry is verified at the coarser L2 mesh, the drag reduction for this mesh is lower than that for the L1 mesh, mostly due to the lower accuracy of the coarse mesh. However, Fig. 5 also shows that when this optimized geometry is verified with a finer L0 mesh the drag reduction of the optimized geometry is well maintained. This shows that it is appropriate to use the 6 million L1 mesh for the final level in the shape optimization.

In Fig. 10, we compare the trimmed optimized wing with the baseline configuration, where the baseline configuration is now trimmed by rotating the tail. We can see that the drag reduction of the optimized configuration is even better relative to this trimmed baseline: 12.1 drag counts (4.1%) lower. We also compute $-\partial C_M / \partial C_L$ for this trimmed optimized configuration: it is 36.52%, slightly higher than the baseline value of 30%.
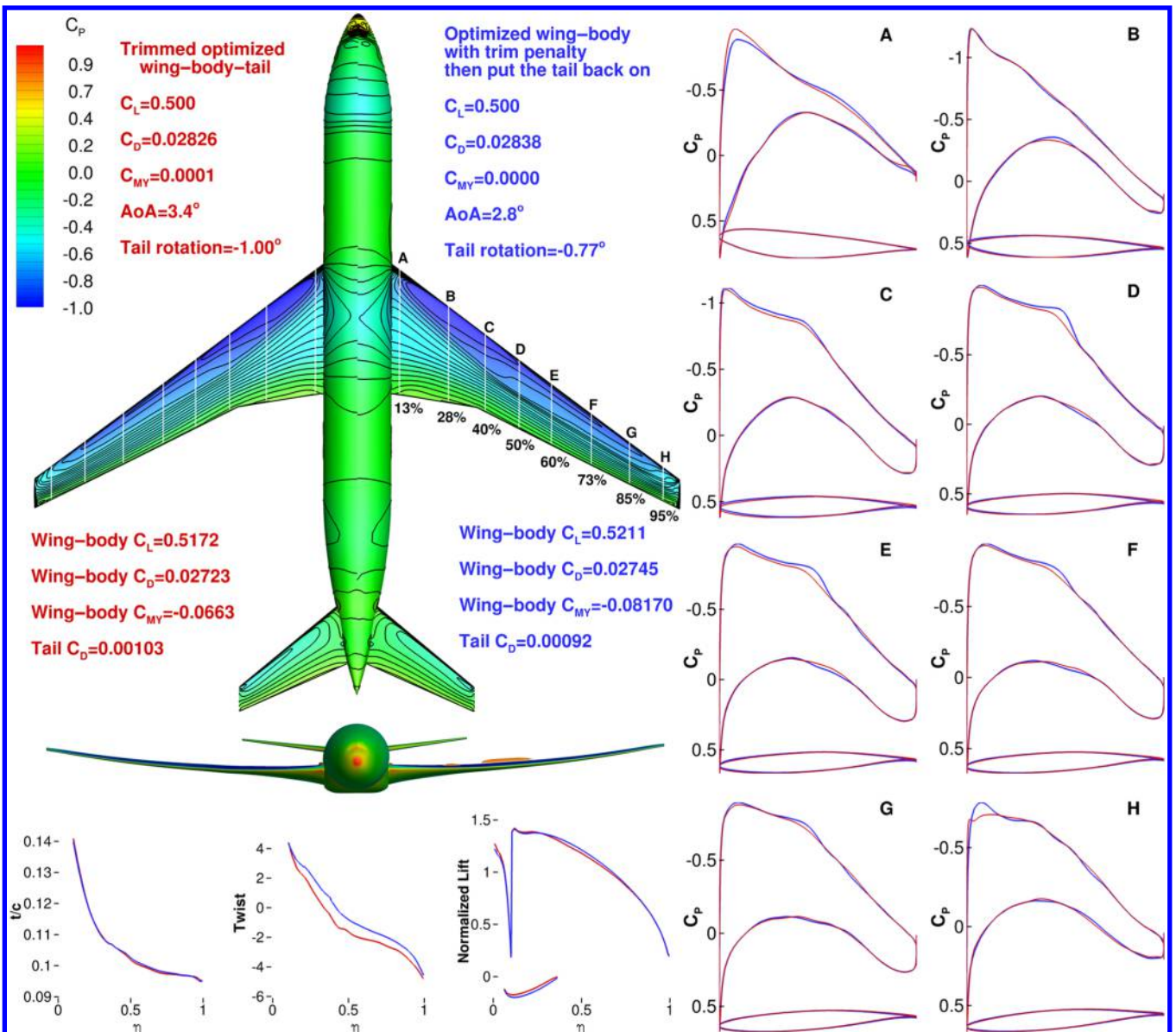

Fig. 16 Comparison of the optimized wing–body with surrogate trim drag penalty and tail added back on (Case 3; right) with the trim-constrained optimized wing–body–tail (Case 2; left).

Recall that we have an optimized configuration without the trim constraint. It is not trimmed within the optimization, but it could be trimmed by tail rotation after the optimization. To investigate the drag increment, we compare the optimized configuration with post-optimization trimming and the trim-constrained optimized configuration. This comparison is shown in Fig. 11. The optimized wing–body–tail without the trim constraint achieve a low drag value (280.4 counts), as described in Sec. IV. However, when we trim it by rotating the tail, the drag increases to 285.6 drag counts, and this increase (5.2 counts) is even higher than that between the untrimmed baseline and the trimmed baseline. Most of the increase comes from the wing rather than the tail, as shown in Fig. 11.

VI.   Case 3: Optimization of Wing with Surrogate Trim Drag Penalty

The goal of this case is to investigate the effect of optimizing the aerodynamic shape of a wing–body configuration without the horizontal tail, while using a trim drag penalty proportional to the pitching moment of the tailless configuration. We also find

the appropriate surrogate for the trim drag variation with respect to the wing–body pitching moment for this configuration.

We construct the trim penalty surrogate model by performing CFD computations on the wing–body–tail configuration for a sequence of tail rotation angles at a fixed lift coefficient ($C_L = 0.5$). By analyzing the forces acting on the separate components (wing, body, and tail), we establish how much drag and lift are required on the tail to trim the wing–body with a certain amount of the pitching moment. By solving the flow with the tail rotation ranging from -10 to 10 deg, we construct the relation of the lift and drag with respect to the moment using one-dimensional (1D) B-spline interpolation, as shown in Fig. 12. The drag, lift, and moment on the tail are all computed with the whole wing–body–tail configuration aircraft reference area (as given by DPW-4) to make the force values on each component consistent and comparable. In the following discussion and figures, we denote the moment generated on the whole wing–body–tail configuration as $C_{M_y}^{wbt}$, the moment on the wing–body as $C_{M_y}^{wb}$, and the moment of the tail as $C_{M_y}^{t}$. We use the same superscript convention for the drag and lift coefficients. Using the 1D B-spline interpolation described previously, we construct the trim penalty surrogate model, which uses the moment generated
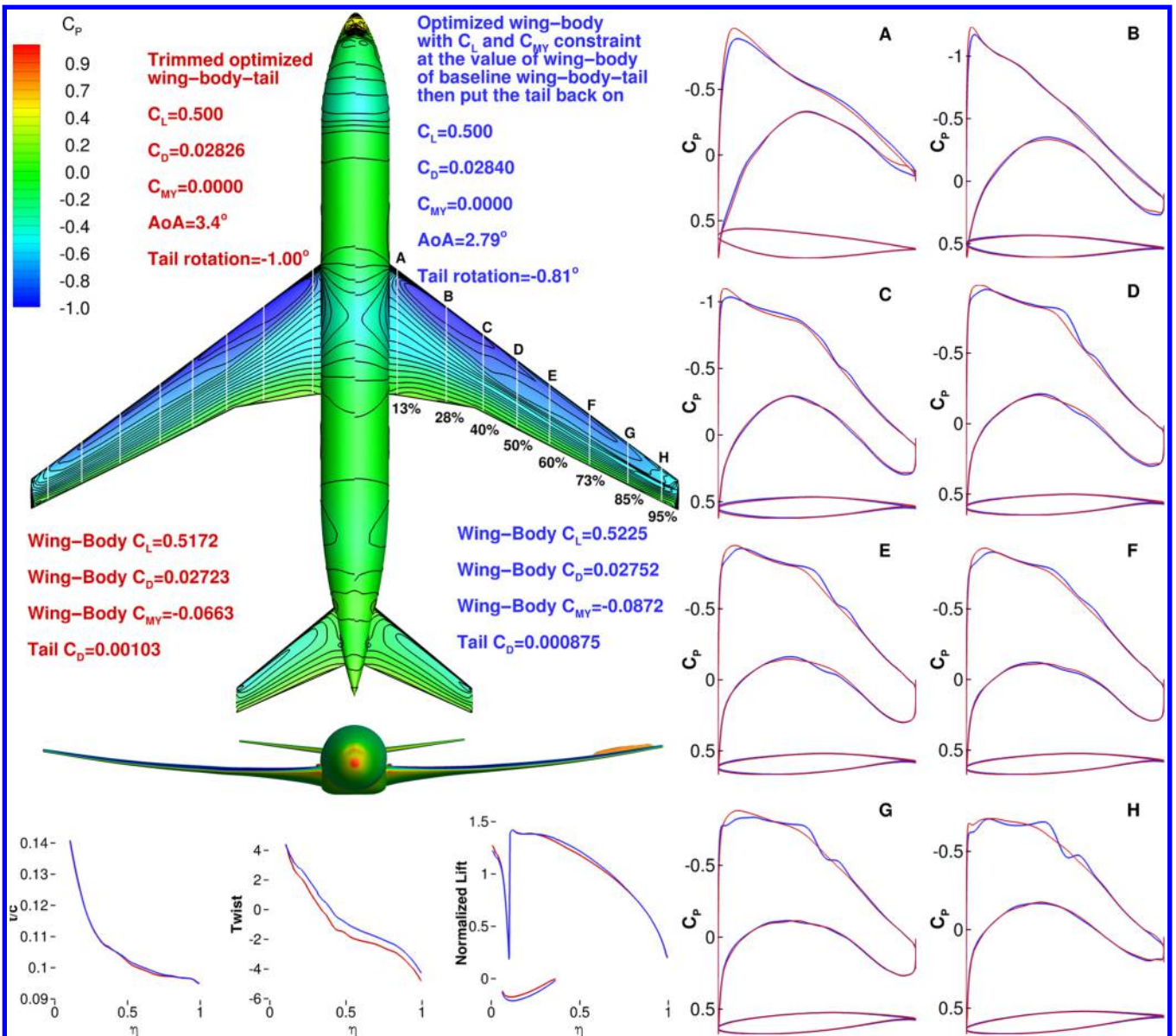

Fig. 17   Comparison of the optimized wing–body–tail with predetermined lift and moment constraints that is trimmed by tail rotation after optimization (Case 4; right) with the trimmed optimized wing–body–tail (Case 2; left).

on the tail to estimate the drag and lift on the tail. This model can be written as

$$
\begin{cases}
C_D^t = f_{C_D}(C_{M_y}^t) \\
C_L^t = f_{C_L}(C_{M_y}^t)
\end{cases}
\tag{1}
$$

In Fig. 12, we can see that the pitching moment generated by the tail varies linearly with the tail lift and that the drag on the tail is nonlinear with respect to the moment. In particular, within the interval $C_{M_y} = [0, 0.2]$, the tail drag decreases as the moment on the tail increases, and the minimum drag on the tail with respect to the moment on the tail is approximately at $C_{M_y} = 0.2$. In addition, since the tail is in the downwash of the wing, to investigate whether this trim penalty relationship would be sensitive to wing lift distribution changes after the optimization, we compute this trim penalty data for the trimmed optimized configuration of the previous section. We show a comparison of this and the baseline, and it turns out that the trim drag penalties for these two designs match well within the interval $C_{M_y} = [0, 0.2]$. The C_{M_y} values on cruise conditions for the wing–body are normally within this range, and the difference in drag is approximately one drag count, so we conclude

that this is a reasonable surrogate model even when the design changes as a result of an optimization.

We also plot the tail rotation angles vs the tail moment on the tail in Fig. 12. The rotation angle for the optimized configuration shifts downward relative to the baseline, and the difference is approximately 1 deg. In the previous section, we established that the cruise angle of attack of the optimized configuration is 3.4 deg, which is 1 deg higher than that of the baseline. This difference in the tail rotation angle is reasonable, since the actual angle of attack of the tail should be the sum of the aircraft angle of attack and its rotation angle.

Given this surrogate model of the trim drag penalty with respect to the required moment to trim the wing–body, we can now optimize the wing–body without the tail while accounting for the drag penalty with this model. For the whole wing–body–tail configuration, the optimization problem is given by

$$
\min \ C_D^{\text{wbt}} \quad \text{subject to } C_L^{\text{wbt}} = 0.5 \quad C_{M_y}^{\text{wbt}} = 0.0
\tag{2}
$$

When we optimize the wing–body with the surrogate model that estimates the drag and lift of the tail, the optimization problem becomes
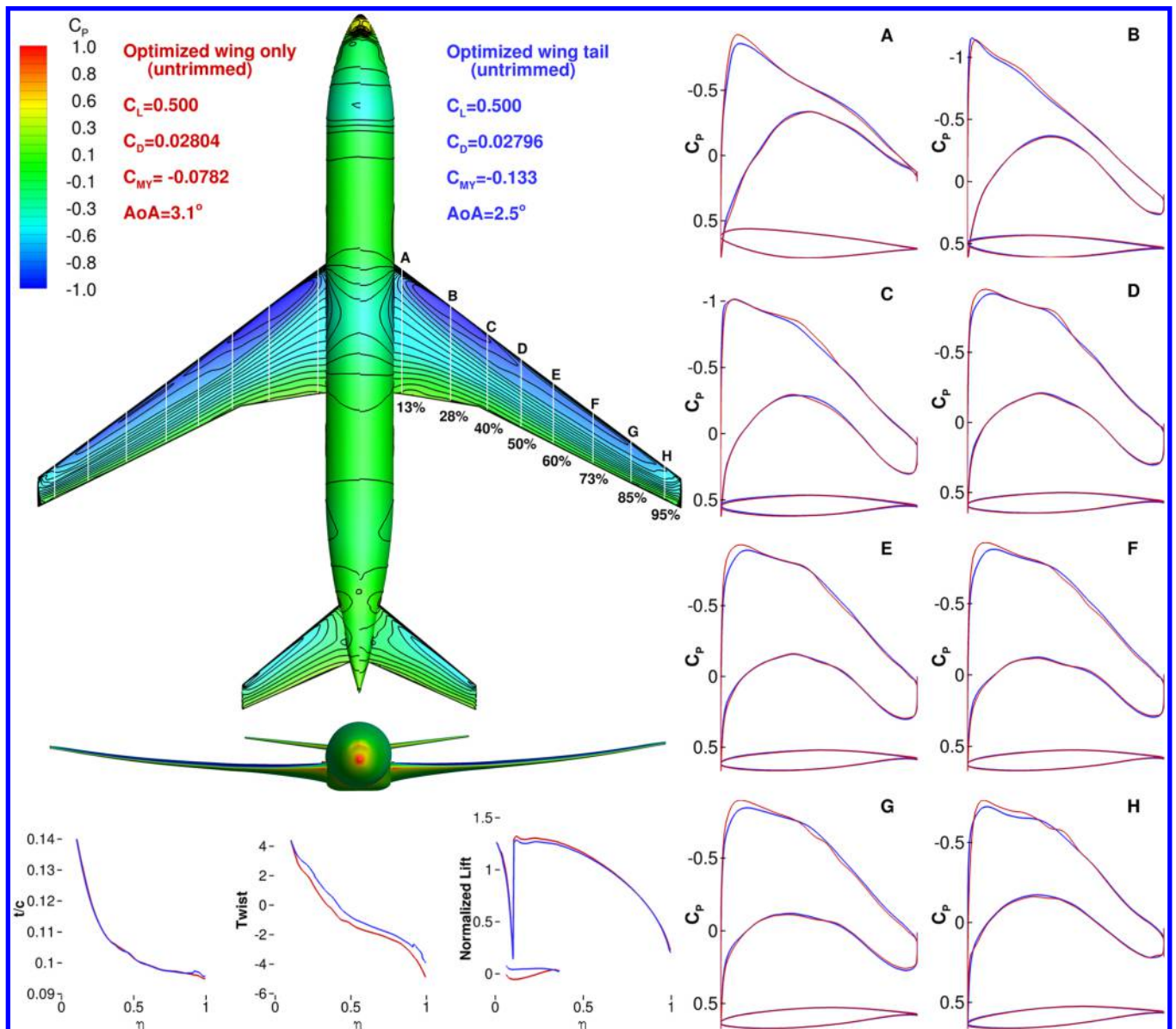

Fig. 18   Comparison of the untrimmed wing optimization (Case 1; left) and untrimmed simultaneously optimized wing–tail configuration (Case 5; right).

$$\min \; C_D^{\text{wb}} + C_D^t \;\; \text{subject to} \;\; C_L^{\text{wb}} + C_L^t = 0.5 \quad C_{M_y}^{\text{wb}} + C_{M_y}^t = 0.0 \qquad (3)$$

where $C_D^t = f_{C_D}(C_{M_y}^t)$ and $C_L^t = f_{C_L}(C_{M_y}^t)$. In this optimization, the mesh for the wing–body–tail is used with hollowed tail blocks to maintain the same mesh topology as far as possible, for a fair comparison. Figure 13 shows the mesh near the tail of the fuselage with and without the tail.

Once we have optimized the wing–body configuration without the tail using the trim drag surrogate, we add the tail back on and trim it. Since we cannot use the estimated tail rotation angle after the wing is optimized, we solve this problem at the target $C_L = 0.5$ with the tail rotation to obtain a new set of data corresponding to this optimized wing–body geometry. To compare the difference in total drag, we recompute the trim penalty data for the new problem. From Fig. 14, we see that the drag penalty is different from that of the baseline and the trimmed optimized wing–body–tail (Case 2) configurations. In the range $C_{M_y} = [0.05, 0.20]$, the drag on the tail of the optimized wing–body is actually higher than that of the other two configurations, and in the range $C_{M_y} = [0.00, 0.05]$, the tail rotation angle curve is approximately in the middle of the other two curves. Figure 15 shows a comparison of the optimized wing–body with estimated drag

penalty and the same configuration with the tail back on. Although the pressure distributions on the two wings are almost the same, the pressure contours on the aft bodies are significantly different. Thus, we believe that the difference in the forces comes primarily from the aft body.

We further compare the optimized wing-body with trim penalty and the tail back on with Case 2. Figure 16 shows this comparison; we see that the pressure distribution of each section is similar. The total drag count of the former configuration is about 1.2 counts higher than that of the latter.

VII.   Case 4: Optimization of Wing with Predetermined Lift and Moment Constraints

We also investigate whether we can achieve a lower drag for the trimmed wing–body–tail by optimizing the wing–body without the tail with predetermined lift and moment constraint values. To this end, we perform another optimization on the wing–body without the tail. Here, C_L is fixed at the value for the wing–body component of the trimmed wing–body–tail baseline, $C_L = 0.5256$, and $C_{M_y} \geq -0.0996$; these are the coefficient values for the wing–body
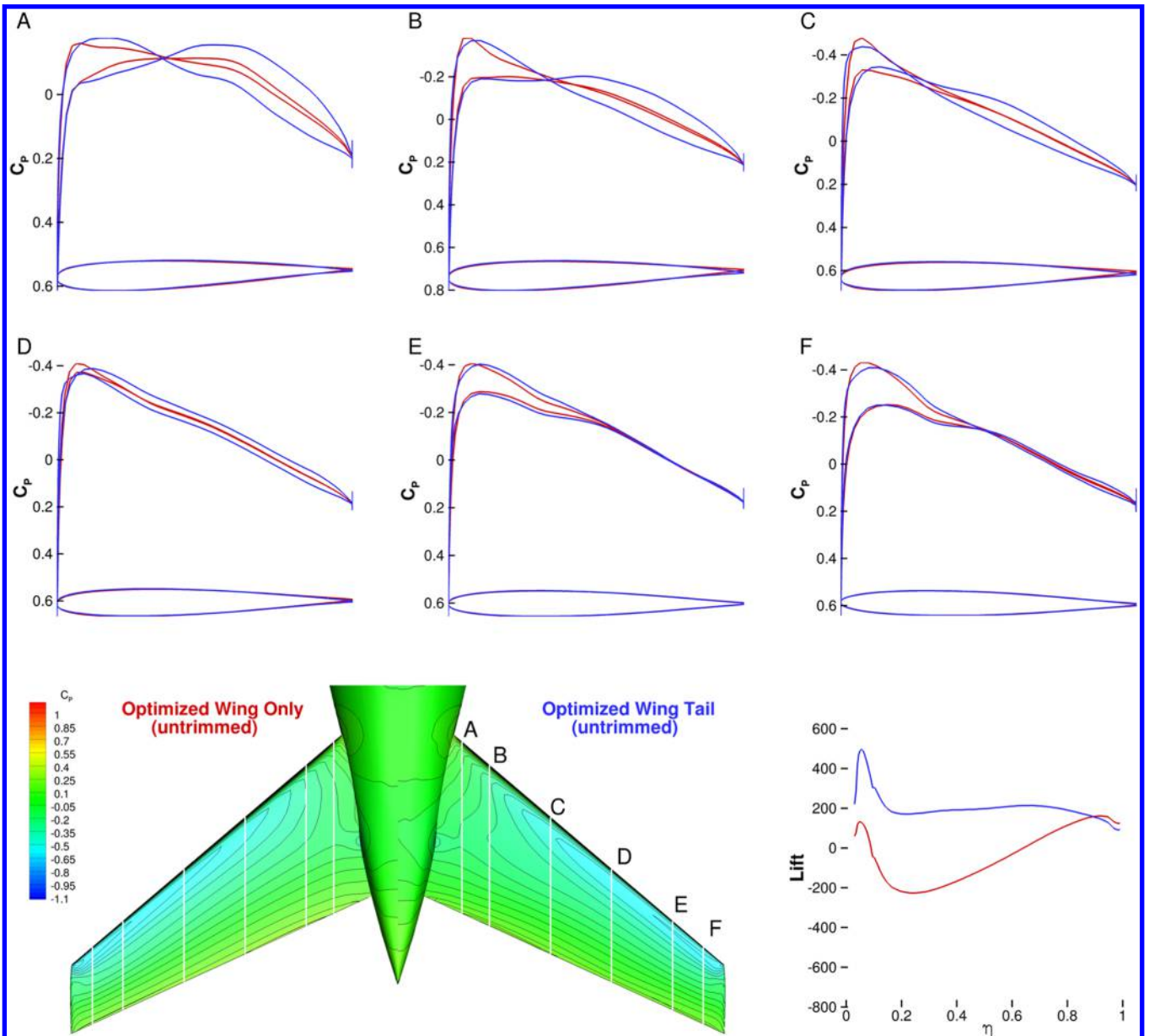

Fig. 19   Comparison of the tail for the untrimmed wing optimization (Case 1; left) and untrimmed simultaneously optimized wing–tail configuration (Case 5; right).

component of the trimmed wing–body–tail baseline. Figure 17 shows a comparison of this optimization (Case 4) with the trim-constrained optimized configuration with the tail (Case 2). The comparison shows that Case 2 still has the lowest drag value; it is about 1.4 drag counts lower than that of the optimized wing–body with the new lift and moment constraints after the addition of the tail for trimming. In addition, a comparison of the normalized lift shows that the lift on the optimized wing–body is higher than that of the trimmed optimized wing–body–tail configuration, which makes it harder for the optimizer to fully eliminate the shock.

From the results presented in this section, we conclude that for single-point aerodynamic shape optimization, the lowest drag is achieved by the trim-constrained wing–body–tail optimization, in which the tail rotation is optimized simultaneously with the wing shape. Optimizing the wing–body without the tail with an estimated tail trim penalty or carefully chosen fixed lift and moment coefficient constraints can also achieve a low drag, but this is one to three drag counts higher than the best.

VIII. Case 5: Optimization of Wing and Tail without Moment Constraint

To quantify the gains that can be obtained by optimizing the wing and horizontal-tail shapes simultaneously, we perform a single-point aerodynamic shape optimization including both wing and tail

shape variables. The total number of shape design variables is $816 + 144 = 960$. This case does not include the tail rotation angle as a design variable, and therefore no trim constraint is enforced.

Figure 18 shows a comparison of the configuration optimized with respect to wing and tail shape simultaneously (Case 5) and that optimized with respect to wing shape alone (Case 1). Both cases are untrimmed. The optimizer reduced the lift on the wing in Case 5 by making the lift on the tail slightly positive. The difference in drag between these two cases is within one drag count, which is relatively small compared with the reduction between the baseline and the wing-only optimized configuration.

The moment coefficient value of Case 5 is $C_{M_y} = -0.133$, the absolute value of which is much higher than that of Case 1 ($C_{M_y} = -0.0782$). Figure 19 shows a comparison of the shape and pressure coefficient distribution on the tail for the two configurations. We see that the optimizer has changed the lift by adding aft loading on the inboard of the tail, while maintaining a similar pressure distribution on the outboard part.

IX. Case 6: Optimization of Wing and Tail with Trim Constraint

In the final case, we add the horizontal tail shape variables to simultaneously optimize the wing shape and the tail shape, hoping to
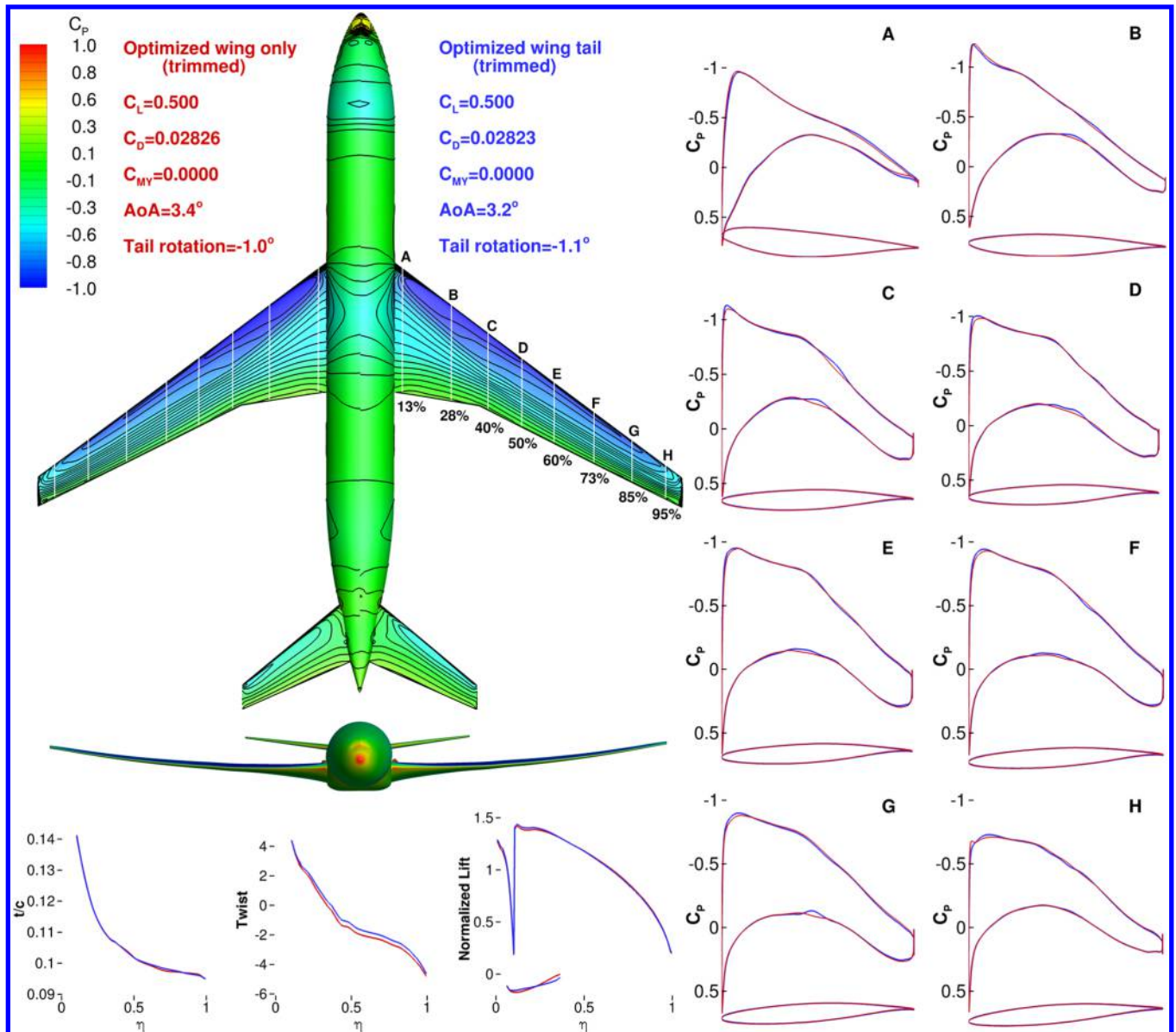

Fig. 20   Comparison of the trimmed wing optimization (Case 2; left) and trimmed simultaneously optimized wing–tail configuration (Case 6; right).
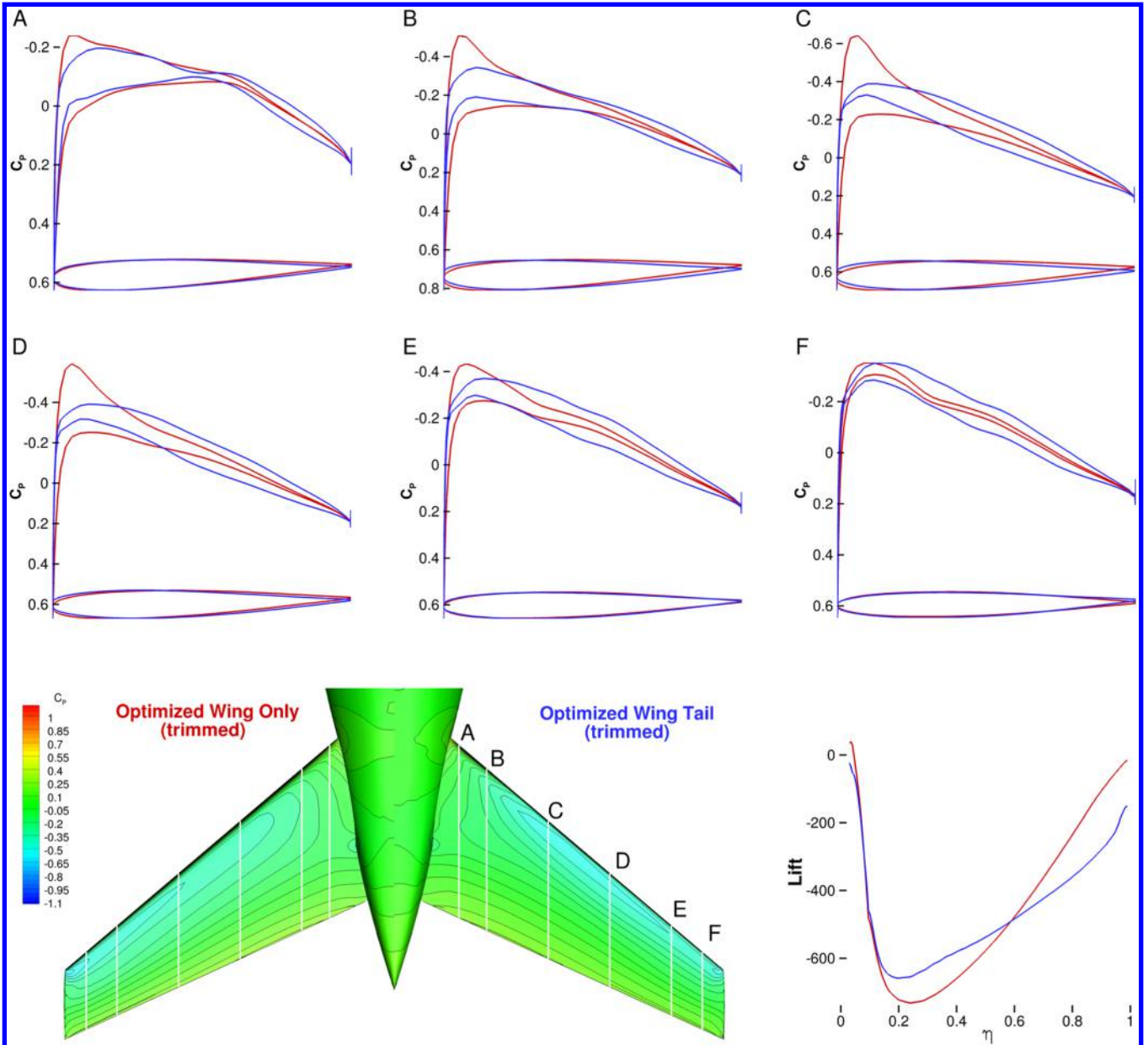
Fig. 21   Comparison of the tail for the trimmed wing optimization (Case 2; left) and trimmed simultaneously optimized wing–tail configuration (Case 6; right).

further improve the aerodynamic efficiency of the full trimmed configuration.

Figure 20 shows a comparison of the trim-constrained wing and tail shape optimization (Case 6) with the trim-constrained wing optimization (Case 2). In this case, the drag reduction is even less than before: approximately 0.3 drag counts. Figure 21 shows that the optimizer has not significantly changed the pressure distribution on the tail, so the lift distribution on the tail varies only slightly. For this

optimized configuration, $-\partial C_M/\partial C_L$ is 35.74%, which is close to the value for the configuration without shape design variables on the tail and higher than the value of the baseline (30%).

X.   Summary of Results

We summarize the comparisons of the baseline and all six optimizations in Table 3, where the dots show whether the tail shape

Table 3   Summary of the optimization studies; all cases satisfy $C_L = 5$, and all optimizations include the wing shape variables as well as the geometric constraints

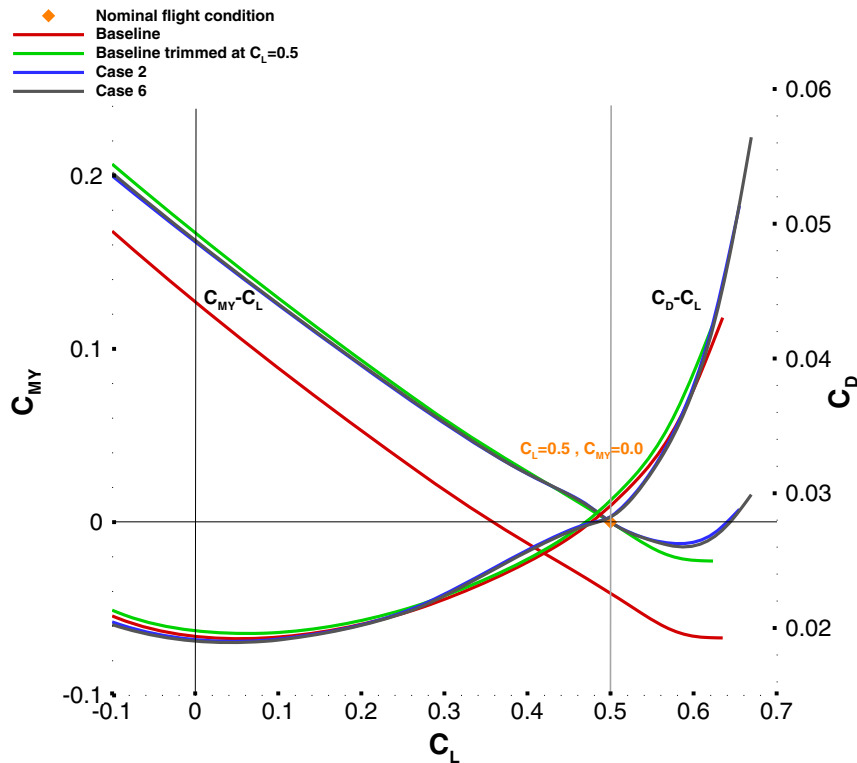| Case	C_D	C_{MY}	Tail shape	Tail rotation	$C_{My} = 0$ constraint	Configuration
Baseline	0.02907	−0.0410				Wing–body–tail
Trimmed baseline	0.02947	0.0		•	•	Wing–body–tail
1	0.02804	−0.0780				Wing–body–tail
2	0.02826	0.0		•	•	Wing–body–tail
3	0.02838	0.0			•	Wing–body
4	0.02840	0.0			•	Wing–body
5	0.02796	−0.1326	•			Wing–body–tail
6	0.02823	0.0	•	•	•	Wing–body–tail

Fig. 22   Comparison of C_{M_y} and C_D vs C_L.

and tail rotation design variables are used, and if the trim constraint is enforced each of the cases. When comparing the results from Cases 3 and 4, we put the tail back on the optimized wing–body and then trimmed it with tail rotation so that the results could be compared with the tail on $C_{My} = 0$; the tail rotation is not a design variable in the optimization. The differences between the optimizations are in the set of design variables and whether or not the moment constraint is enforced. Enforcing a trim constraint and using tail rotation achieves a lower drag value than that for the cases in which the trim penalty is estimated or a fixed-value moment constraint is used. When the trim constraint is present, adding shape design variables on the tail does not reduce the overall drag significantly; it results in a drag reduction of 0.3 counts.

Figure 22 compares the C_{M_y}–C_L curve with the C_D–C_L curve for four of the configurations: baseline, trimmed baseline, Case 2, and Case 6. This plot shows that the baseline curve shifts up when trimmed and that the optimized configurations maintain nearly the same trend and slope within the linear region. Around the nominal flight condition, the optimized configurations exhibit a slight nonlinear behavior, while the baseline maintains a linear trend. In addition, as C_L increases, the C_{M_y} for both optimized configurations curves up earlier than the baseline. In the $C_D - C_L$ curve, both of the optimized configurations have a lower drag than the baseline at around the design C_L. However, the optimized configurations sacrifice performance at lower C_L values, from 0.25 to 0.47.

XI.   Conclusions

In this work, we set out to find the value of including trim during the aerodynamic shape optimization of a conventional aircraft configuration. To this end, we performed a series of optimizations of the Common Research Model wing–body–tail and wing–body configurations. We minimized the drag coefficient subject to the lift, pitching moment, and geometric constraints. The optimizations were performed on two mesh levels with 746,000 and 5.97 million cells, using 816 shape design variables on the wing and 144 shape design variables on the tail, together with angle of attack and horizontal tail rotation angle.

Of the optimizations that included trim constraints, the one with tail rotation as a design variable achieved the lowest overall drag. The single-point trim-constrained optimization was 12.1 drag counts lower than the trimmed baseline, which amounts to 4.1% of the total drag of the trimmed baseline.

The aerodynamic shape optimization of the wing–body without the tail was performed by implementing a surrogate model of the trim drag penalty to account for the tradeoff between the wing performance and the trim drag penalty. When we added the tail back on the optimized wing–body with this trim penalty, the configuration was 1.2 drag counts higher than the trim-constrained optimized wing–body–tail. Thus, if such drag-coefficient differences are important to the designer, the trim-constrained optimization with the horizontal tail rotation is preferred. Otherwise, the designer can use the trim drag surrogate model to get results that are approximate.

When we added the shape design variables for the tail, the trim-constrained optimization reduced the drag by only 0.3 counts. Overall, these results show that the baseline Common Research Model configuration is already well designed from the trim point of view, with a reasonable wing moment coefficient. The value of considering trim in aerodynamic shape optimization would increase further if we considered multiple center-of-gravity positions or if we started from a baseline wing with a larger pitchdown moment.

References

[1] Jameson, A., "Aerodynamic Design via Control Theory," *Journal of Scientific Computing*, Vol. 3, No. 3, Sept. 1988, pp. 233–260.
doi:10.1007/BF01061285

[2] Peter, J. E. V., and Dwight, R. P., "Numerical Sensitivity Analysis for Aerodynamic Optimization: A Survey of Approaches," *Computers and Fluids*, Vol. 39, No. 3, 2010, pp. 373–391.
doi:10.1016/j.compfluid.2009.09.013

[3] Lyu, Z., Kenway, G. K., and Martins, J. R. R. A., "Aerodynamic Shape Optimization Studies on the Common Research Model Wing Benchmark," *AIAA Journal*, Vol. 53, No. 4, April 2015, pp. 968–985.
doi:10.2514/1.J053318

[4] Lyu, Z., and Martins, J. R. R. A., "Aerodynamic Design Optimization Studies of a Blended-Wing-Body Aircraft," *Journal of Aircraft*, Vol. 51, No. 5, Sept. 2014, pp. 1604–1617.
doi:10.2514/1.C032491

[5] Kroo, I., "Tail Sizing for Fuel Efficient Transports," *AIAA Aircraft Design, Systems and Technology Meeting*, AIAA Paper 1983-2476, Oct. 1983.
doi:10.2514/6.1983-2476

[6] Lyu, Z., Kenway, G. K., Paige, C., and Martins, J. R. R. A., "Automatic Differentiation Adjoint of the Reynolds-Averaged Navier–Stokes Equations with a Turbulence Model," *21st AIAA Computational Fluid Dynamics Conference*, AIAA Paper 2013-2581, July 2013.
doi:10.2514/6.2013-2581

[7] Vassberg, J. C., DeHaan, M. A., Rivers, S. M., and Wahls, R. A., "Development of a Common Research Model for Applied CFD Validation Studies," AIAA Paper 2008-6919, 2008.

[8] Reuther, J. J., Jameson, A., Alonso, J. J., Rimlinger, M. J., and Saunders, D., "Constrained Multipoint Aerodynamic Shape Optimization Using an Adjoint Formulation and Parallel Computers, Part 1," *Journal of Aircraft*, Vol. 36, No. 1, 1999, pp. 51–60.
doi:10.2514/2.2413

[9] Reuther, J. J., Jameson, A., Alonso, J. J., Rimlinger, M. J., and Saunders, D., "Constrained Multipoint Aerodynamic Shape Optimization Using an Adjoint Formulation and Parallel Computers, Part 2," *Journal of Aircraft*, Vol. 36, No. 1, 1999, pp. 61–74.
doi:10.2514/2.2414

[10] Nielsen, E. J., and Anderson, W. K., "Aerodynamic Design Optimization on Unstructured Meshes Using the Navier–Stokes Equations," *AIAA Journal*, Vol. 37, No. 11, 1999, pp. 1411–1419.
doi:10.2514/2.640

[11] Bueno-Orovio, A., Castro, C., Palacios, F., and Zuazua, E., "Continuous Adjoint Approach for the Spalart–Allmaras Model in Aerodynamic Optimization," *AIAA Journal*, Vol. 50, No. 3, 2012, pp. 631–646.
doi:10.2514/1.J051307

[12] Hicken, J. E., and Zingg, D. W., "Induced-Drag Minimization of Nonplanar Geometries Based on the Euler Equations," *AIAA Journal*, Vol. 48, No. 11, 2010, pp. 2564–2575.
doi:10.2514/1.J050379

[13] Vassberg, J., and Jameson, A., "Influence of Shape Parameterization on Aerodynamic Shape Optimization," von Kármán Inst. for Fluid Dynamics, TR , Brussels, Belgium, April 2014.

[14] Telidetzki, K., Osusky, L., and Zingg, D. W., "Application of Jetstream to a Suite of Aerodynamic Shape Optimization Problems," *52nd Aerospace Sciences Meeting*, AIAA Paper 2014-0571, Feb. 2014.
doi:10.2514/6.2014-0571

[15] Carrier, G., Destarac, D., Dumont, A., Meheut, M., Din, I. S. E., Peter, J., Khelil, S. B., Brezillon, J., and Pestana, M., "Gradient-Based Aerodynamic Optimization with the elsA Software," *52nd Aerospace Sciences Meeting*, AIAA Paper 2014-0568, Feb. 2014.
doi:10.2514/6.2014-0568

[16] Liem, R., Kenway, G. K. W., and Martins, J. R. R. A., "Multimission Aircraft Fuel Burn Minimization via Multipoint Aerostructural Optimization," *AIAA Journal*, Vol. 53, No. 1, Jan. 2015, pp. 104–122.
doi:10.2514/1.J052940

[17] Kenway, G. K. W., and Martins, J. R. R. A., "Multipoint High-Fidelity Aerostructural Optimization of a Transport Aircraft Configuration," *Journal of Aircraft*, Vol. 51, No. 1, Jan. 2014, pp. 144–160.
doi:10.2514/1.C032150

[18] Mader, C. A., and Martins, J. R. R. A., "Stability-Constrained Aerodynamic Shape Optimization of Flying Wings," *Journal of Aircraft*, Vol. 50, No. 5, Sept. 2013, pp. 1431–1449.
doi:10.2514/1.C031956

[19] Cliff, S. E., Reuther, J. J., Saunders, D. A., and Hicks, R. M., "Single-Point and Multipoint Aerodynamic Shape Optimization of High-Speed Civil Transport," *Journal of Aircraft*, Vol. 38, No. 6, 2001, pp. 997–1005.
doi:10.2514/2.2886

[20] Laitone, E. V., "Ideal Tail Load for Minimum Aircraft Drag," *Journal of Aircraft*, Vol. 15, No. 3, March 2006, pp. 190–192.
doi:10.2514/3.58339

[21] Phillips, W. F., Hansen, A. B., and Nelson, W. M., "Effects of Tail Dihedral on Static Stability," *Journal of Aircraft*, Vol. 43, No. 6, 2006, pp. 1829–1837.
doi:10.2514/1.20683

[22] Kenway, G. K. W., Kennedy, G. J., and Martins, J. R. R. A., "Scalable Parallel Approach for High-Fidelity Steady-State Aeroelastic Analysis and Derivative Computations," *AIAA Journal*, Vol. 52, No. 5, May 2014, pp. 935–951.
doi:10.2514/1.J052255

[23] Kenway, G. K. W., Kennedy, G. J., and Martins, J. R. R. A., "Aerostructural Optimization of the Common Research Model Configuration," *15th AIAA/ISSMO Multidisciplinary Analysis and Optimization Conference*, AIAA Paper 2014-3274, June 2014.

[24] Kenway, G. K., Kennedy, G. J., and Martins, J. R. R. A., "A CAD-Free Approach to High-Fidelity Aerostructural Optimization," *Proceedings of the 13th AIAA/ISSMO Multidisciplinary Analysis Optimization Conference*, AIAA Paper 2010-9231, Sept. 2010.

[25] van der Weide, E., Kalitzin, G., Schluter, J., and Alonso, J. J., "Unsteady Turbomachinery Computations Using Massively Parallel Platforms," *Proceedings of the 44th AIAA Aerospace Sciences Meeting and Exhibit*, AIAA Paper 2006-0421, 2006.

[26] Jameson, A., Schmidt, W., and Turkel, E., "Numerical Solution of the Euler Equations by Finite Volume Methods Using Runge–Kutta Time Stepping Schemes," AIAA Paper 1981-1259, 1981.

[27] Saad, Y., and Schultz, M. H., "GMRES: A Generalized Minimal Residual Algorithm for Solving Nonsymmetric Linear Systems," *SIAM Journal on Scientific and Statistical Computing*, Vol. 7, No. 3, 1986, pp. 856–869.
doi:10.1137/0907058

[28] Balay, S., Gropp, W. D., McInnes, L. C., and Smith, B. F., *Efficient Management of Parallelism in Object Oriented Numerical Software Libraries*, Birkhäuser Boston, Cambridge, MA, 1997, pp. 163–202.

[29] Balay, S., Brown, J., Buschelman, K., Eijkhout, V., Gropp, W. D., Kaushik, D., Knepley, M. G., McInnes, L. C., Smith, B. F., and Zhang, H., "PETSc User's Manual," Argonne National Library TR ANL-95/11, Rev. 3.4, 2013.

[30] Gill, P. E., Murray, W., and Saunders, M. A., "SNOPT: An SQP Algorithm for Large-Scale Constrained Optimization," *SIAM Journal of Optimization*, Vol. 12, No. 4, 2002, pp. 979–1006.
doi:10.1137/S1052623499350013

[31] Perez, R. E., Jansen, P. W., and Martins, J. R. R. A., "pyOpt: A Python-Based Object-Oriented Framework for Nonlinear Constrained Optimization," *Structural and Multidisciplinary Optimization*, Vol. 45, No. 1, Jan. 2012, pp. 101–118.
doi:10.1007/s00158-011-0666-3

[32] Lyu, Z., Kenway, G. K. W., and Martins, J. R. R. A., "RANS-based Aerodynamic Shape Optimization Investigations of the Common Research Model Wing," *Proceedings of the AIAA Science and Technology Forum and Exposition (SciTech)*, AIAA Paper 2014-0567, Jan. 2014.
doi:10.2514/6.2014-0567

[33] Roache, P. J., "Verification of Codes and Calculations," *AIAA Journal*, Vol. 36, No. 5, 1998, pp. 696–702.
doi:10.2514/2.457

[34] Lovely, D., and Haimes, R., "Shock Detection from Computational Fluid Dynamics Results," *Proceedings of the 14th Computational Fluid Dynamics Conference*, AIAA Paper 1999-3285, 1999.

[35] Walatka, P. P., Buning, P. G., Pierce, L., and Elson, P. A., *PLOT3D User's Manual*, NASA TM-101067, March 1990.

This article has been cited by:

1. Časlav Ilić. Comparison of Optimizer-Based and Flow Solver-Based Trimming in the Context of High-Fidelity Aerodynamic Optimization 455-465. [Crossref]

2. James G. Coder, David Hue, Gaetan Kenway, Thomas H. Pulliam, Anthony J. Sclafani, Leonel Serrano, John C. Vassberg. Contributions to the Sixth Drag Prediction Workshop Using Structured, Overset Grid Methods. *Journal of Aircraft*, ahead of print1-14. [Abstract] [Full Text] [PDF] [PDF Plus]

3. Justin Gray, Jeffrey Chin, Tristan Hearn, Eric Hendricks, Thomas Lavelle, Joaquim R. R. A. Martins. 2017. Chemical-Equilibrium Analysis with Adjoint Derivatives for Propulsion Cycle Analysis. *Journal of Propulsion and Power* 33:5, 1041-1052. [Abstract] [Full Text] [PDF] [PDF Plus]

4. Nathalie Bartoli, Thierry Lefebvre, Sylvain Dubreuil, Romain Olivanti, Nicolas Bons, Joaquim Martins, Mohamed-Amine Bouhlel, Joseph Morlier. An adaptive optimization strategy based on mixture of experts for wing aerodynamic design optimization . [Citation] [PDF] [PDF Plus]

5. Timothy R. Brooks, Gaetan K. Kenway, Joaquim Martins. Undeflected Common Research Model (uCRM): An Aerostructural Model for the Study of High Aspect Ratio Transport Aircraft Wings . [Citation] [PDF] [PDF Plus]

6. Orest Mykhaskiv, Pavanakumar Mohanamuraly, Jens-Dominik Mueller, Shenren Xu, Sebastian Timme. CAD-based shape optimisation of the NASA CRM wing-body intersection using differentiated CAD-kernel . [Citation] [PDF] [PDF Plus]

7. Andrei Merle, Arthur Stueck, Arne Rempke. An Adjoint-based Aerodynamic Shape Optimization Strategy for Trimmed Aircraft with Active Engines . [Citation] [PDF] [PDF Plus]

8. Gaetan K. W. Kenway, Joaquim R. R. A. Martins. 2017. Buffet-Onset Constraint Formulation for Aerodynamic Shape Optimization. *AIAA Journal* 55:6, 1930-1947. [Abstract] [Full Text] [PDF] [PDF Plus]

9. Nitin Garg, Gaetan K.W. Kenway, Joaquim R.R.A. Martins, Yin Lu Young. 2017. High-fidelity multipoint hydrostructural optimization of a 3-D hydrofoil. *Journal of Fluids and Structures* 71, 15-39. [Crossref]

10. Zhi-Qiang Wan, Xiao-Zhe Wang, Chao Yang. 2017. Integrated aerodynamics/structure/stability optimization of large aircraft in conceptual design. *Proceedings of the Institution of Mechanical Engineers, Part G: Journal of Aerospace Engineering* 095441001668714. [Crossref]

11. James G. Coder, Thomas H. Pulliam, David Hue, Gaetan K. Kenway, Anthony J. Sclafani. Contributions to the 6th AIAA CFD Drag Prediction Workshop Using Structured Grid Methods . [Citation] [PDF] [PDF Plus]

12. Gaetan K. Kenway, Asitav Mishra, Ney R. Secco, Karthikeyan Duraisamy, Joaquim Martins. An Efficient Parallel Overset Method for Aerodynamic Shape Optimization . [Citation] [PDF] [PDF Plus]

13. Lorenzo Travaglini, Sergio Ricci, Giampiero Bindolino. 2016. PyPAD: a multidisciplinary framework for preliminary airframe design. *Aircraft Engineering and Aerospace Technology* 88:5, 649-664. [Crossref]

14. David A. Burdette, Gaetan K. Kenway, Joaquim Martins. Aerostructural design optimization of a continuous morphing trailing edge aircraft for improved mission performance . [Citation] [PDF] [PDF Plus]

15. Gaetan K. Kenway, Joaquim Martins. Aerodynamic Shape Optimization of the CRM Configuration Including Buffet-Onset Conditions . [Citation] [PDF] [PDF Plus]

16. David Koo, David W. Zingg. Progress in Aerodynamic Shape Optimization Based on the Reynolds-Averaged Navier-Stokes Equations . [Citation] [PDF] [PDF Plus]

17. Gaetan K. W. Kenway, Joaquim R. R. A. Martins. 2016. Multipoint Aerodynamic Shape Optimization Investigations of the Common Research Model Wing. *AIAA Journal* 54:1, 113-128. [Abstract] [Full Text] [PDF] [PDF Plus] [Supplemental Material]